DOUBLE DIFFERENTIAL CONTINUUM NEUTRON SCATTERING CROSS SECTIONS IN IRON AND NICKEL FOR INCIDENT ENERGIES OF 7.5, 10 AND 12 MEV

by

ALBERT GEORGE BEYERLE, JR.

A thesis submitted to the Graduate Faculty of
North Carolina State University at Raleigh
in partial fulfillment of the
requirements for the Degree of
Doctor of Philosophy

DEPARTMENT OF PHYSICS

RALEIGH

1 9 8 1

APPROVED BY:

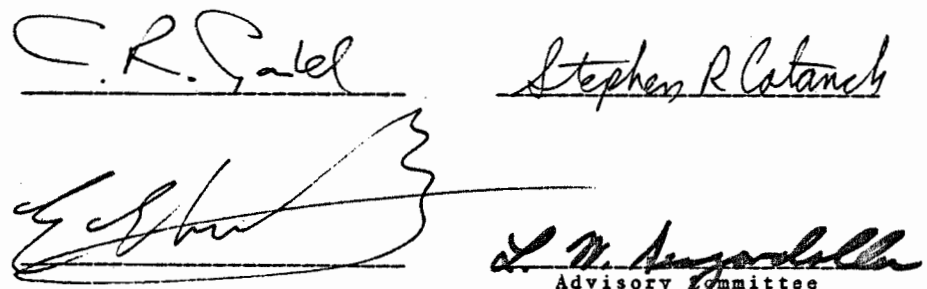

Advisory Committee
Chairman

BIOGRAPHY

Albert George Beyerle, Jr. was born in Baltimore, Maryland on August 14, 1953. He was raised in Baltimore County and later near Annapolis, Maryland where he graduated from Annapolis Senior High School in June 1971.

The author entered North Carolina State University and received a Bachelor of Science degree in physics in May of 1975. He entered graduate school in physics at North Carolina State University, accepting a teaching assistantship, and later a research assistantship to pursue the research described herein.

The author has been married to the former Maren Oline Schmidt since December 1974. Maren Beyerle received a Bachelor of Science degree in Psychology from the University of North Carolina at Chapel Hill in May 1978.

TABLE OF CONTENTS

Page

LIST OF SYMBOLS v

I Introduction 1

II Experimental Procedure 5

2.1 Physical Apparatus 5

2.2 Electronics 22

III Data Reduction 33

3.1 Data Acquisition Program 33

3.2 Experimental Procedure 34

3.3 Offline Procedures 45

3.4 Normalization 52

IV Data Correction 54

4.1 Need for Data Correction 54

4.2 Approach to the Problem 59

4.3 Features of EFFIGYC 61

4.4 Method 65

4.5 Solution of the Multiple Scattering Problem . . 68

4.6 Iteration of Cross Section 72

V Analysis and Results 79

5.1 The Energy Distribution 79

5.2 Decay of the Compound System 81

5.3 Presentation of the Data 88

5.4 Discussion of the Uncertainties 110

5.5 Conclusion 114

Appendix A Multiple Scattering Rate Derivation 117

Appendix B Experimental Data 123

B.1 Iron at 7.5 MeV 123

B.2 Iron at 10 MeV 125

B.3 Iron at 12 MeV 127

B.4 Nickel at 7.5 MeV 129

B.5 Nickel at 10 MeV 131

B.6 Nickel at 12 MeV 133

LIST OF REFERENCES 135

SYMBOLS

B_b^a = Integrated beam current collected on the beam stop used for normalization purposes. The superscript "a" indicates the gas situation (in or out) and the subscript "b" indicates sample position. Further discussion of the meanings of sample in/out and gas in/out can be found in Chapter III.

BIAS = Number added to each channel each time a difference is taken to ensure that no negative values are obtained (usually BIAS=100).

C = Undefined constant.

C_b^a = Experimental counts with superscript "a" noting the gas situation and subscript "b" indicates sample situation.

${}_Z^A C$ = Compound nucleus with A nucleons and Z protons.

E_c = Compound nucleus excitation energy formed by the capture of a neutron by the target nucleus.

E_r = Energy of the residual nucleus after decay of the compound system by the emission of a neutron.

E_n = Energy of the incident neutrons in these experiments.

ΔE = Energy difference between the ground states of the target or residual nucleus and the compound nucleus.

ε, E_{out} = In Chapter V, ε is the energy of the emitted

neutrons which is equal to E_{out}.

E_i = Energy incident to the i^{th} order process.

E_a = Energy of a neutron as detected from the material denoted by subscript a. The value of a is "s" for the scattering sample or "poly" for the polyethylene normalization sample.

F = Functional describing the scattering process.

F^{-1} = Inverse of F

$f(x)$ = Function describing scattering process such that $\int_x f(x)\,dx = F$

F_{ab} = relative flux from source point a to sample point b.

g = The number of spin states for the neutron (=2).

h = Planck's constant divided by 2π.

L_b^a = Detection system live time to clock time ratio. This serves as a correction for system dead time.

m_n = Mass of a neutron.

n_a = Number of atoms in the sample denoted by subscript a. Meaning of a is defined with the symbol E_a.

N = number of test points chosen in Monte Carlo evaluation of an integral.

N_a = Count rate in the sample, denoted by the subscript a, defined as the number of counts in the experiment divided by the experimental integrated beam current. This is in fact the

experimental difference as defined in equation 3.1.

P_c = Production of neutrons in the solid material of the gas cell itself.

$P_d(\varepsilon)$ = Probability of decay of the compound system as a function of emitted neutron energy. This defines the shape of the energy spectra.

P_g = Production of neutrons in the gas contained within the cell.

r_{ab} = Distance between points a and b.

$\bar{r}_{ab}$ = Vector from point a to point b.

$\bar{r}^{i}_{ab}$ = Same as $\bar{r}_{ab}$ except superscript i denotes that this a vector associated with the i^{th} discrete test point.

$\bar{r}_a$ = Vector from origin to point a.

r_o = Radius of a single nucleon.

R = Total rate of scattering from all order processes.

$^{A}_{Z}R$ = Residual nucleus with A nucleons and Z protons.

R_i = Rate of scattering from ith order process.

$R_c(\varepsilon)$ = Rate of compound nucleus formation from the excited residual nucleus. This is not an observed process but a conceptual device.

$R_d(\varepsilon)$ = Rate of compound nucleus decay to the excited residual system.

R_p = Pearson linear correlation coefficient.

S_c = Defined as the logarithm (base e) of the compound system level density ($S_c = \ln(\rho_c)$).

S_r = Defined as the logarithm (base e) of the residual system level density ($S_r = \ln(\rho_r)$).

S_s = Scattering of neutrons from the sample.

S_x = Scattering of neutrons from things surrounding the sample but excluding the sample itself.

$S(t;E)$ = Beam resolution function. This includes both time and energy dispersion.

T = Nuclear temperature parameter.

${}^{A}_{Z}T$ = Target nucleus with A nucleons and Z protons.

T_{ab} = transmission from source point a to sample point b.

T_{in} = Transmission probability for a neutron into the target nucleus.

v = Velocity

V = Volume

V_i = Volume of integration for the ith order scattering process used in the evaluation of the scattering rates.

V_{samp} = Volume of the scattering sample.

x = Multiplication operation.

η = Detector efficiency

Δ = Difference between the observed cross section (σ_{obs}) and the simulation based on the estimated cross section (σ_{est}).

Ω = Solid angle in steradians.

ρ_c = Level density of the compound system.

ρ_d = Level density available to the decay of the compound system which is the density of states available to the residual nucleus plus neutron.

ρ_r = Level density in the residual system.

σ = Cross section

σ_s^{bu} = Source breakup cross section.

σ_{est} = Estimate of continuum scattering cross section, based on the results of previous simulation.

σ_c = Cross section for the capture of a neutron by the target or residual nucleus.

σ^i = Cross section of i^{th} process. For example elastic, or inelastic scattering.

σ_i = Cross section of the i^{th} order process. For example, single or double scattering.

σ_{new} = New guess for estimated cross section for update of σ_{est}.

σ_{obs} = Observed cross section. This is the uncorrected experimental result which is to be put into EFFIGYC for correction.

σ_s = Source cross section.

σ_{total} = Total cross section for all types of interactions.

$\langle\ \rangle$ = Average of the enclosed quantity.

I Introduction

Neutron double differential scattering cross sections ($d^2\sigma/d\Omega dE_{out}$) exciting unresolvable high-lying levels in natural-abundance elemental iron and nickel nuclei have been measured for incident neutron energies between 7.5 and 12 MeV. Energy distributions for outgoing neutron energies above 0.5 MeV and up to about 2 MeV below the incident energy have been measured. These are referred to as "continuum" scattering measurements since we can not resolve the individual levels of the residual nuclei in these experiments due to the large number of closely spaced levels and we must deal with the collective properties of many such levels. Some of this work has been previously reported[1,2]. Our experiment and results are described here in detail.

This experiment fits in with the TUNL program of scattering measurements. Discrete scattering studies to low-lying resolvable levels have been previously carried out at TUNL by Hogue[3] and Glendinning[4] and are still being carried out for medium mass nuclei by El-Kadi[5]. The continuum measurements represent a new phase for the TUNL neutron scattering program.

The idea of continuum scattering is not new. These measurements have been made in the incident neutron energy range below 7.5 MeV for example by Towle and Owen[6], Thomson[7], Wilenzick[8], and Kinney[9] and at around 14 MeV, for example by Stengl et. al.[10] and Mather et. al[11]. Experimental difficulties have prevented the filling of the area between 7.5 and 12 MeV. Only recently has this gap begun to close due to measurements such as ours and for example those by Drake et. al.[12] or Biryukov et. al.[13] In principle, the measurements of the angular and energy distributions are not difficult. If neutrons of the desired energy strike a sample of scattering material from a known direction, then detectors placed at various angles with respect to the incident neutrons can be used to measure the angular and energy distributions of the scattered neutrons and thereby arrive at scattering cross sections. Unfortunately this ideal experiment can not be carried out. Properties of neutrons and their interactions with matter introduce many complications that are difficult to account for. Paramount among these are neutron production and detection difficulties.

Neutrons produced by material other than the desired source and undesirable neutrons from even the best sources are complicating factors. In fact, the lack of a monoenergetic neutron source is the principal reason for the

lack of data in this energy range. The fact that there is no neutron detector for these neutrons which will give direct energy information, as there is for charged particles or electromagnetic radiation, requires that time-of-flight techniques must be used for energy spectroscopy. Detection efficiencies which depend on neutron energy and response of the detection material to gamma rays also complicate neutron detection. In addition, large scattering samples and scattering materials other than the sample material in the vicinity of the sample (air for example) add further complications. In as much as is possible, these complicating factors have been accounted for experimentally. This is accomplished by careful experimental design and experimental isolation and measurement of as many of the undesirable effects as possible. However, some of the effects must be removed by calculation. As will be discussed, the calculation of the neutron source complications are one of the most unique features of these measurements. These calculations are carried out by the computer program EFFIGYC.

The motivation for these measurements is two-fold. Iron and nickel are important structural materials for fusion reactor design and cross section data are necessary for all energies below 14 MeV (the energy carried away by the neutron in a low energy $T(d,n)^4He$ reaction). These data

also provide level density information on nuclei and serve to bridge the 7.5 to 14 MeV gap in data where other channels ((n,2n), (n,np)) begin to open up and may effect the results.

II Experimental Procedure

2.1 Physical Apparatus

In order to carry out neutron scattering measurements, neutrons are produced by source reactions involving high velocity charged particles. To produce these charged particle beams, the TUNL direct extraction negative ion source (DENIS II) is used. This source delivered about 85 μA of negative hydrogen ions of which about 1 μA was delivered on the charged particle target. The ion beam is passed through a radio-frequency "chopper" which subjects the beam to a transverse electric field that is varying sinusoidally with time at a frequency of 2 MHz. The resulting transverse displacement, sweeps the beam across a 0.375 inch aperture located in the beam tube. This produces a beam pulse every 250 nsec. An auxiliary chopper removes all but every fourth pulse by application of a transverse electric field square-wave tuned to sweep the pulses out of the acceptance of the beam optics system. This yields pulses every 1 micro-second. These pulses are "bunched" by application of a longitudinal electric field, sinusoidally varying in time, which decelerates the leading part of the pulse and accelerates the trailing part to compress or bunch

the beam into a very narrow pulse. Typical beam pulse widths on target are about 2 nsec full width at half maximum.

Beam pulses are accelerated, charge changed, and further accelerated by the TUNL tandem Van de Graaff accelerator. The positively charged particle beam so produced is transported to the target via the 38° beam line to the neutron time-of-flight scattering area. Details of the TUNL ion sources, accelerator, and beam transport systems have been previously described[14,3,4,15].

For reasons to be discussed later, some of these experiments require the use of tritium gas which is radioactive. The use of the relatively large amounts of radioactive gas contained by a gas cell and a thin foil requires careful measures to minimize radiation hazards to the environment. The tritium safety system has been discussed in detail by Purser[16] and briefly by Seagondollar[15].

Neutrons are produced, by charged particle bombardment of appropriate nuclei, in a gas volume contained at the end of the beam line in a gas cell (the accelerator target). In this work two gas cells were used. The first cell has been discussed elsewhere[3]. This cell contains deuterium gas, and

is made of thin-walled stainless steel, as illustrated in figure 2.1. The inside of the cell is lined with a removable tantalum liner and has a tantalum beam stop to reduce neutron backgrounds from the cell materials. The cell is sealed from the beam line and outside atmosphere with an indium "O" ring. It is pressurized to 30 psia with high purity deuterium which has been passed through a liquid nitrogen trap before entering the cell to remove hydrocarbon contaminates. This cell is used to produce neutrons via the $D(d,n)^3He$ reaction.

The second cell is used exclusively for tritium gas to minimize contamination of the tritium system with other hydrogen isotopes. It is illustrated in figure 2.2. The cell[15] is constructed of thin walled stainless steel and contains a tantalum liner. Neutrons are produced in this cell by the $T(p,n)^3He$ reaction. Since the protons impinging on the cell walls at the proton energies needed copiously produce neutrons, the choice of those cell materials which are struck by the protons is particularly important. Studies of this matter have been carried out by Drosg, et. al.[17] with the conclusion that Ni^{58} is the best material for the beam stop. A Ni^{58} beam stop is used in this cell. The entrance foil, which is molybdenum, is cemented in place with epoxy glue as a seal from the beam line vacuum. Molybdenum entrance foils are used rather than ^{58}Ni due to

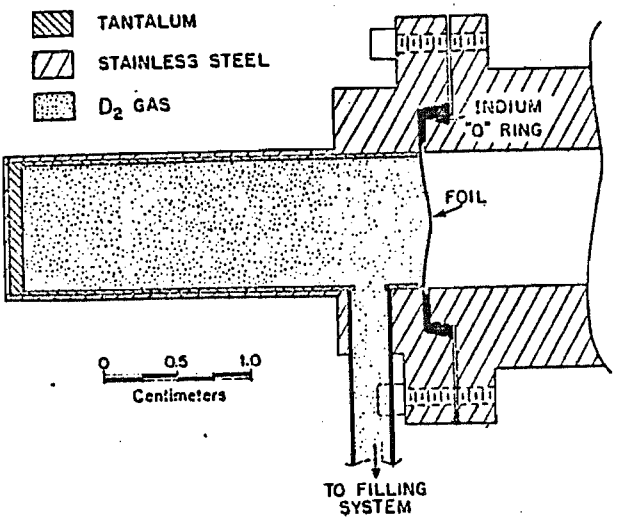

Figure 2.1 Deuterium gas cell

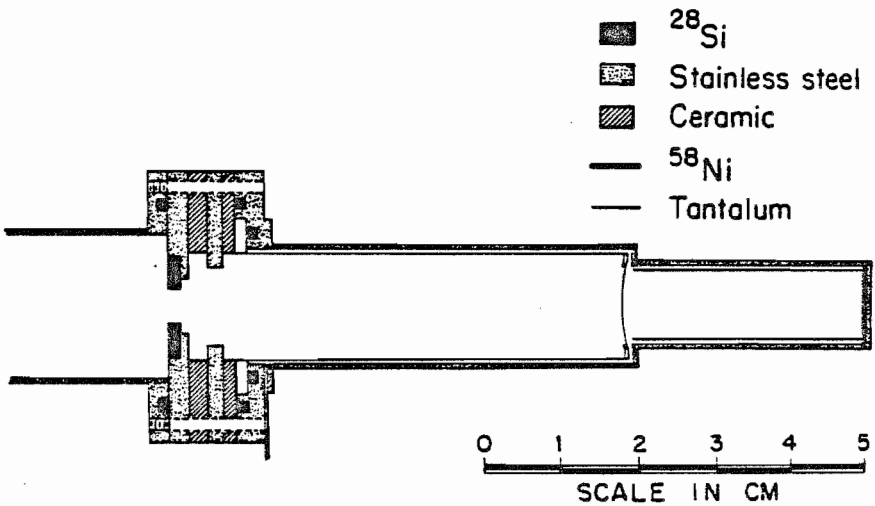

Figure 2.2 Tritium gas cell

difficulties with the quality of the Ni foils and the greater relative danger of a foil rupture. The tritium is prevented from escaping to the outside environment by two "viton" "O" rings. Before the cell is pressurized with T_2, it is tested statically with 3 atmospheres (45 psia) of He gas for foil leaks and then for at least 30 minutes with twice the beam used in the data taking run. Then the cell is filled with tritium gas which is stored in a uranium furnace. (Tritium is stored in the form of UT_3 in a furnace of sintered uranium powder. The tritium is liberated by the heating of the furnace and can be recaptured by allowing it to enter the cool furnace. Other gasses, particularly the reaction by-products, are easily removed since the tritium storage system will store only hydrogen. At present the tritium contains about 10-15% H_2 and an insignificant amount of D_2 gas.)

The choice of the neutron source reaction is critical for these measurements. To avoid extremely difficult problems in data analysis, it is highly desirable to do these experiments with monoenergetic neutrons. Unfortunately all neutron producing reactions in the energy range of this work produce some neutrons of energy lower than that of the primary neutron group. The lower energy neutrons from our sources must be minimized as they cannot be accounted for experimentally. (Experimental efforts to account for other

lower energy neutrons produced by things other than the source gas will be discussed in Chapter III.) The most nearly monoenergetic source reactions are those involving isotopes of hydrogen. Reactions involving heavier elements all may lead to bound excited states in the residual nucleus and thus lead to more than one discrete neutron group. For these measurements, the $D(d,n)^3He$ and the $T(p,n)^3He$ reactions are used as they produce the most nearly monoenergetic neutrons in the correct energy range. These source reactions have been studied extensively at Los Alamos Scientific Laboratory[18] and at TUNL[19] for this energy range.

The D(d,n) reaction has been used for the 7.5 MeV neutron energy data. The threshold for deuteron breakup (D(d,p+n)D) corresponds to about 7.5 MeV neutron energy. The deuterons can breakup on the heavier elements of the cell itself at these energies but these breakup effects can be accounted for experimentally. Therefore the breakup of the source gas deuterons is not a problem at this energy. The D(d,n) reaction has the advantage that its cross section is higher and the angular distribution of the neutrons is more forward peaked. This results in a neutron flux at our scattering sample that is about a factor of three higher than that of our other choice, the T(p,n) reaction. The more forward-peaked angular distribution also reduces the room-scattered background by producing relatively fewer

neutrons which do not scatter off of the sample. An example of a D(d,n) time-of-flight source spectrum is shown in figure 2.3.

The $T(p,n)^3He$ reaction is used for the higher incident neutron energies of 10 and 12 MeV. As shown in figure 2.4, the ratio of production cross section for source gas breakup neutrons to that of the primary neutrons rises faster in the D(d,n) source[18]. We feel that the lower neutron production cross sections and higher isotropy of the T(p,n) source is offset by the fact that the experimentally unsubtractable gas breakup background is substantially less for this reaction. It should be pointed out that the T(p,n) reaction is not much better than the D(d,n) reaction if all undesired neutrons are taken into account. The T(p,n) reaction produces many neutrons from the gas container and also many gamma rays. These backgrounds, though large, are experimentally subtractable. A typical $T(p,n)^3He$ 0° source time-of-flight spectrum is shown in figure 2.5. It was obtained with one of the main detectors at 0° with no scattering sample in place.

Scattering samples used in this work are of natural elemental material. All samples are cylindrical and are mounted on a wire co-axial with the pivot axis of the detectors. The geometry is shown in figure 2.6. Samples

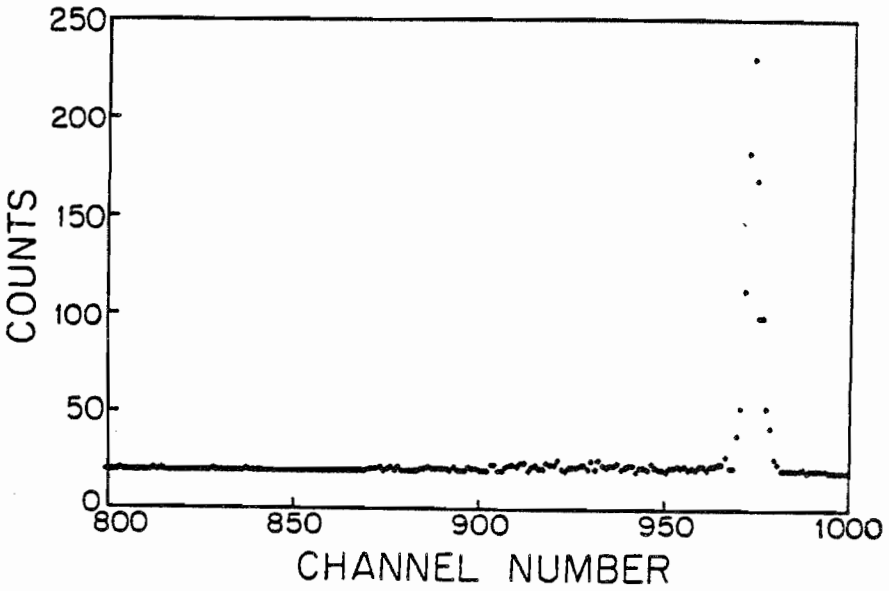

Figure 2.3 Neutron energy distributions from the $D(d,n)^3He$ source reaction at 0° for primary neutron energy of 7.5 MeV. Note that there are no gas-breakup neutrons.

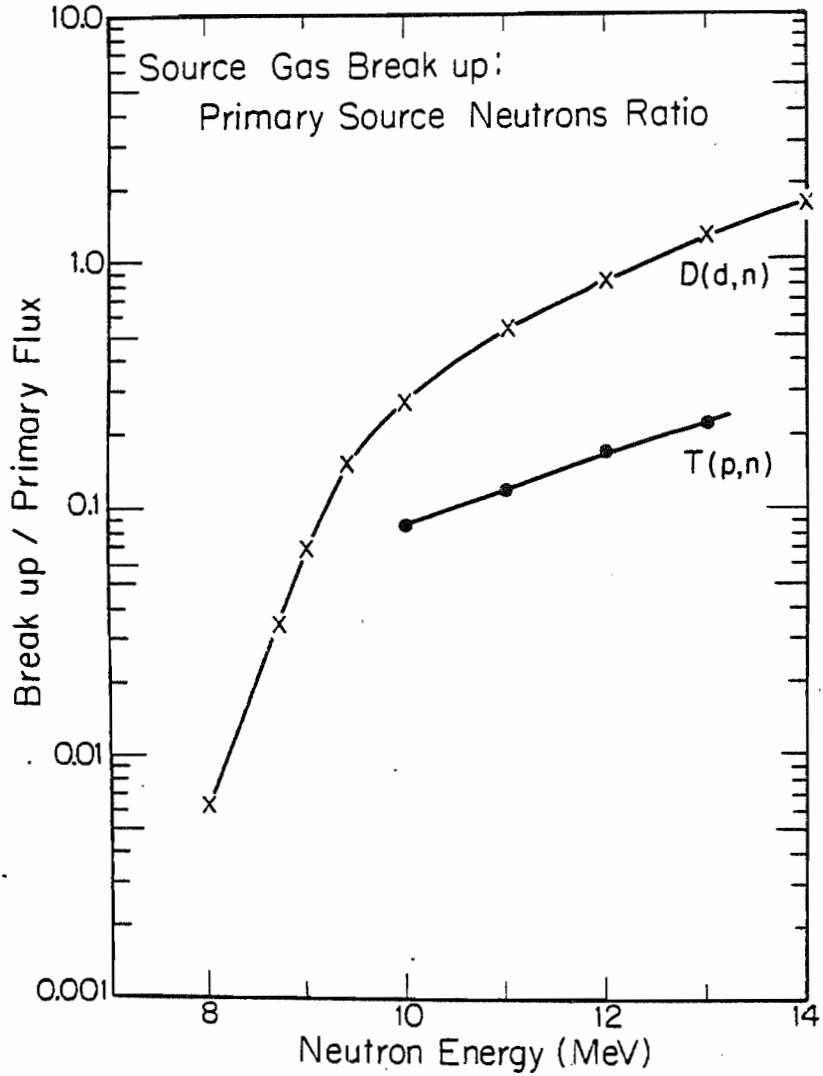

Figure 2.4 Ratio of gas breakup neutrons to primary source neutrons as a function of primary neutron energy. This is the component if the noise-to-signal ratio which cannot be accounted for experimentally.

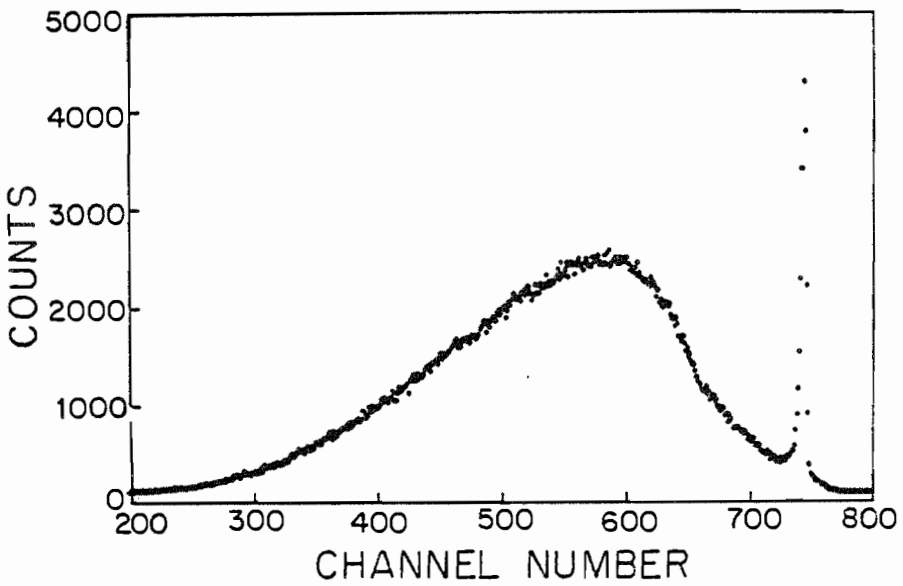

Figure 2.5 Typical $T(p,n)^3He$ 0^o source neutron energy distribution at 12 MeV primary neutron energy. Note that the source is not monoenergetic with the low energy component primarily due to neutron produced in the cell walls.

have a 3 centimeter outside diameter, are hollow with a 1.3 centimeter diameter hole along the sample symmetry axis, and are 4.4 centimeters in height. The nickel sample has a mass of 230.5 grams and the iron cylinder has a mass of 202.7 grams. The wire is hung over precisely located pulleys on the ceiling and just over the detector goniometer table. Tension is kept in the upper pulley with a weight attached to the upper end of the wire. The wire may be moved up and down with a stepping motor with up to four samples located along the wire. This allows positioning of scattering samples remotely. A Zeiss optical level is used to check of the proper centering the samples. The samples may also be computer driven allowing the automatic positioning of the samples by entering the sample desired. This system allows positioning of the sample to within 1/80 inch.

Neutrons are detected with massively shielded NE213 liquid scintillators. Time-of-flight techniques (TOF) are used to determine the energy of scattered neutrons. The main detectors are located on carriages which allow radial positioning of the scintillators from 2.5 to 3.9 meters for the "4-meter" detector and 2.5 to 5.7 meters for the "6-meter" detector. For the present experiments, the detector distances are set at 2.76 and 3.76-meters for the "4-meter" and "6-meter" respectively. All liquid scintillators are 2 inches in depth. The main scintillators

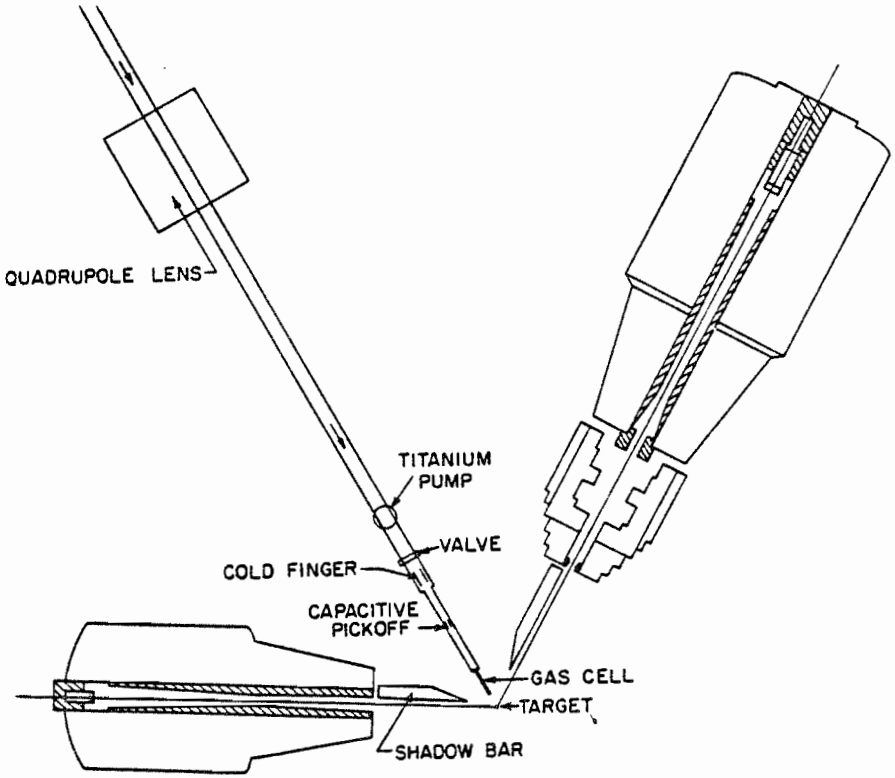

Figure 2.6 Scattering geometry. Shows location of detectors, shadow bars, scattering sample (or target), gas cell, and various beam line components.

are 3.5 inches and 5 inches in diameter for the "4-meter" and "6-meter" detectors respectively. The continuum flight paths are chosen to allow slow neutrons from a given burst to arrive at the "6-meter" detector before the fastest neutrons from the next beam burst can catch up with them and the "4-meter" is placed to achieve approximately the same count rate as the "6-meter".

The "6-meter" detector shield assembly is shown in cross section in figure 2.7, and the "4-meter" shield, while a bit shorter in axial length, is very similar (see Hogue [3] and Glendinning [4]). The shields weigh about 5000Kg and contain primarily a mixture of paraffin and lithium carbonate as described by Glasgow[20]. The throat of the detector contains a doubly-truncated conical collimator to reduce in-scattering effects. The collimator is designed so that a neutron that scatters from the front quarter of the collimator cannot reach the detector without passing through additional collimator material as it will be screened by that part of the collimator closer to the detector. The back three-fourths of the collimator is designed so that neutrons entering the front of the detector cannot strike this portion of the collimator directly. Also the collimator must not screen any of the sample from any of the detector yet shield as much of the detector as possible from neutrons other than those which scatter from the sample. In

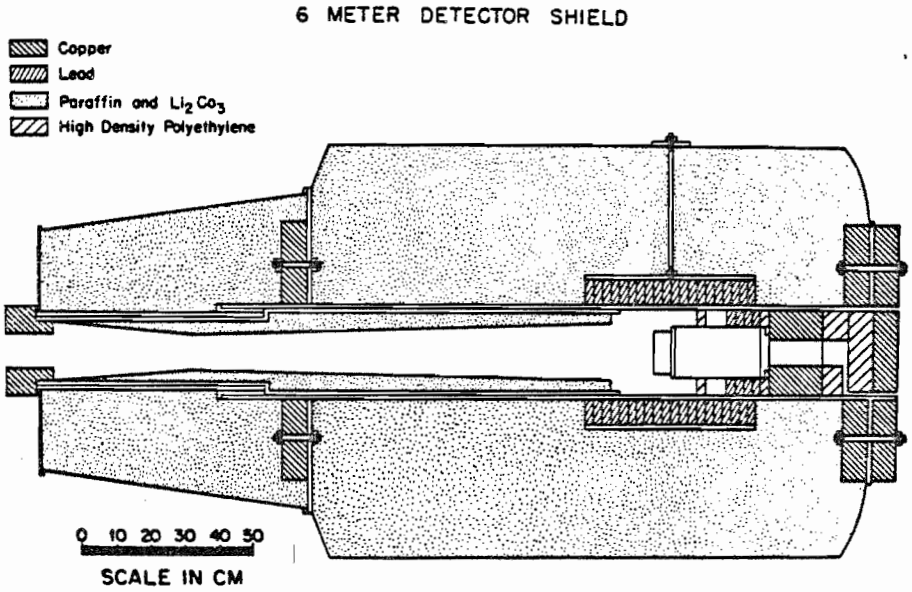

Figure 2.7 Cross section view of the "6-meter" neutron detector and its shield.

this manner the collimator allows no neutron to scatter from the collimator and still reach the detector without either passing through additional collimator material or scattering more than once. A detailed analysis of such doubly-truncated collimators was made by Glasgow[20]. Behind the scintillator is copper and high-density polyethylene in the "6-meter" and paraffin and copper in the "4-meter" detector. More paraffin behind the "4-meter" detector is added at the beginning of each run to provide additional shielding. This is made necessary for the low-bias measurements because fast neutrons may scatter from the walls of the target area and reach the detector at the same time as slower, low energy neutrons directly from the scattering sample.

The massive detector shield assemblies are mounted on carriages which pivot about the scattering sample axis. Detector angles are measured by verniers located on the goniometer. To enable movement of these shields, each carriage is driven by an electric motor mounted on the rear of the carriages and controlled near the pivot axis.

In addition to the main detectors, there are two monitor detectors. A flux monitor is located about two meters from the gas cell, mounted on the ceiling at a neutron production angle relative to the beam axis of 90 degrees. This

detector, tightly collimated and viewing only the gas cell directly, serves as a neutron flux monitor. It is inside a copper shield which is much smaller than the main detector shields. Another monitor detector, located at zero degrees and about four meters from the gas cell, is unshielded, and serves as a 'timing' monitor. Its purpose is to check changes in timing, both in resolution and zero-point drifts. These items will be discussed in Chapter III.

Both main detectors are used with massive tungsten shadow bars. Shadow bars are positioned so that (1) direct neutron flux from the gas target to the detectors must pass through as much of the shadow bar as possible to attenuate the flux, (2) the shadow bar must not interfere with the detectors view of the sample, (3) 'in-scattering' must be minimized, and (4) the shadow bar must be placed so that the other detector can not 'see' it. This last requirement requires placing the detectors more than 180 degrees apart or both at very forward angles (less than about 35^{o} for each detector). 'In-scattering' here means the process where neutrons scatter from both the sample and shadow bar and then into the detector. It is extremely important to remove these 'in-scattering' effects because their contribution can not be accounted for by any of our data taking or analysis procedures. The optimuum positions of the shadow bars depends upon the angular positions of the detectors. A

mechanical system has been built which simplifies moving each shadow bar into its proper position. With this system the shadow bars need only be set up by hand once at the beginning of each run. Mechanical details of the detector and shadow bar systems have been covered in more detail by Seagondollar[15].

The detectors themselves are standard NE-213 liquid scintillators coupled to Ampex XP2041 photomultiplier tubes for the large scintillators and RCA 8575 photomultiplier tubes for the monitors. NE-213 was chosen because of its good pulse shape discrimination properties and fast signal response. The pulse shape discrimination system will be discussed in more detail with the electronics system in section 2.2. The photomultiplier tube bases are ORTEC standard bases for the monitors and count-rate stabilized bases for the main detectors. We have been unable to detect gain shifts for any count rates used in these experiments (typically less than 3000 counts per second at the detectors).

2.2 Electronics

The electronics for each of the detectors is essentially the same. To allow the continuum neutron emission

measurements the TUNL time-of-flight electronics had to be redesigned. The most significant improvement has been the incorporation of the Canberra model 2160 pulse-shape discrimination[21,22] modules (PSD). The wide dynamic range of these modules allows PSD of the pulses due to low recoil energy events in the scintillation liquid without saturation for the high energy events. The fast response of these units can eliminate n-gamma selection as a factor in the dead-time of the system.

The only variation in electronics between the detectors is that the monitor detectors do not have an automatic cable switch while the main detectors do. (The automatic cable switch is a co-axial relay which is controlled manually by a switch or placed under computer control.) A block diagram of the electronics is shown in figure 2.8. Figure 2.9 shows the time of occurrence of various signals in the electronics with lettered keys indicating where the signals may be found. These various test points will be discussed in the text. Fast signals from the photomultiplier anode enter the control room area via RG-8 50 ohm cable [A] and are split into the Canberra 2160 PSD module, the Canberra 1428 constant fraction discriminator (CFD), and the ORTEC 490B amplifier-single channel analyzer (AMP-SCA). The PSD module is the beginning of the pulse shape analysis part of the system that is used to minimize the gamma-ray background in

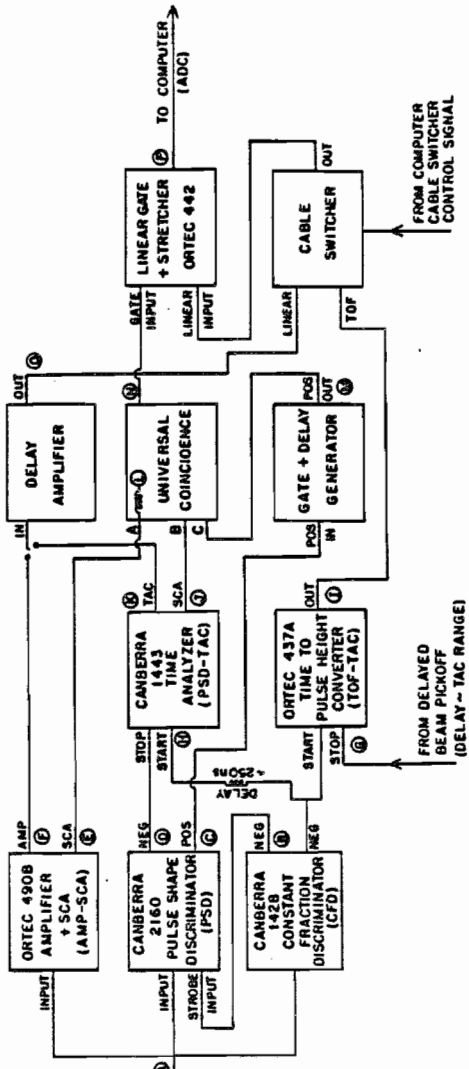

Figure 2.8 Diagram of the electronics for one of the main detectors.

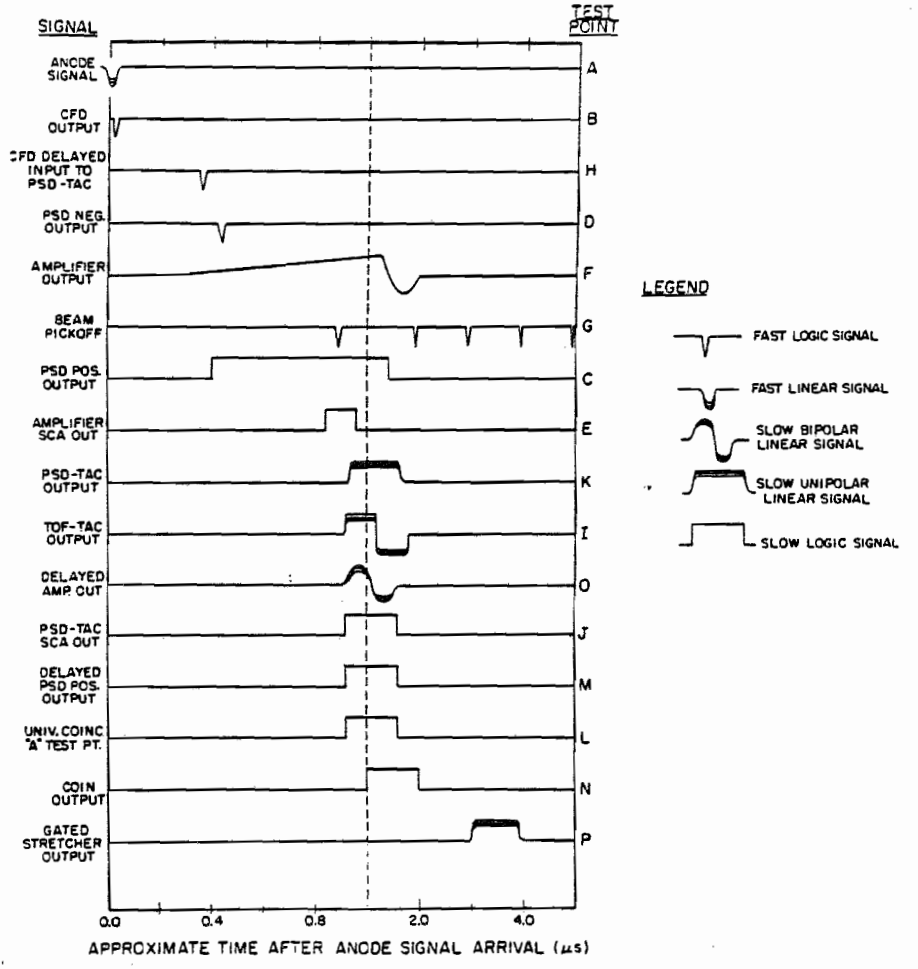

Figure 2.9 Timing diagram for various signals in the time-of-flight electronics. Test points are the same as those in figure 2.8 and in the text.

the spectra. The CFD picks off the timing information from the anode signal of the photomultiplier base and defines the lower cutoff level for the recoil energies during low bias operation of the system. The AMP-SCA shapes the fast negative anode signal into a slow bipolar pulse [F] which the slow electronics in the system can handle and defines the bias during high bias operation. The terms "high bias" and "low bias" refer to two different modes of operation for different types of measurements and will be discussed below in the description of how the bias is set. The time-of-flight information is derived from an ORTEC 437A time-to-amplitude coverter (TOF-TAC) whose start signal comes from the CFD [B], triggered by the detector anode signal, and a stop signal [G] derived from the time of arrival of the beam pulse near the cell with a capacitive pick-off just upstream of the cell. This pickoff feeds an amplifier, and CFD (not shown). The beam pick-off signal must be delayed since the beam actually arrives at the beam capacitive pick-off before the neutrons arrive at the detector. The signals are turned around in this manner because the pick-off signals arrive at the TOF-TAC every 1 micro-second in this configuration and use of the pick-off to start the TAC would start the TAC every microsecond, causing the TAC to become paralyzed. Signals out of the TOF-TAC [I] have an amplitude linearly related to the time between the start and stop signals fed into it. The output of the TOF-TAC is fed into an automatic

cable switch to a linear gate which verifies the requirements for a valid neutron-induced pulse.

The PSD is carried out in the center branch of the electronics. The CFD output serves as the start [B] for the PSD-TAC and output pulses from the PSD module operated in the n+gamma mode, serve as stop-pulse for a CANBERRA 1443 PSD-TAC [D]. The PSD module operated in the n+gamma mode, produces an output pulse for every input related in time to the peak of the anode signal. Since the CFD triggers at a time corresponding to a constant fraction of the way up the anode signal pulse, the time between these two signals [B,D] is a measure of the rise time of the pulse. Since neutrons interact in the scintillation detector primarily with protons and gamma rays with electrons, the rise time of the pulses is different. A window is set on the output of the PSD-TAC (internal to the PSD-TAC) such that only output voltages between two predefined levels will produce a logic signal [J] corresponding to the rise time of a neutron-induced pulse in the detector. An example of a PSD spectrum is shown in figure 2.10.

The top branch of the electronics processes the linear information carried in the anode signal. The AMP-SCA combination produces both a linear signal and a logic signal which carries the high bias information. The linear output

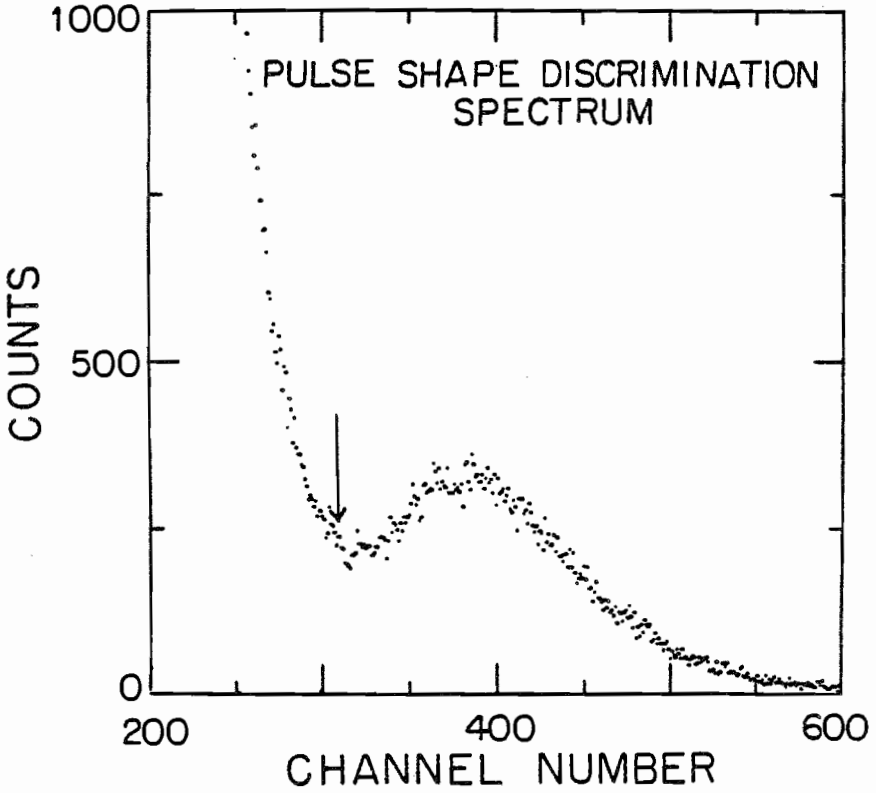

Figure 2.10 Sample pulse-shape discrimination spectrum at low bias. Lower level set for separation of neutrons and gammas is shown by the arrow.

of the AMP-SCA [F] or the linear output of the PSD-TAC [K] is delayed [O] to bring it into time sychronization with the TOF-TAC [I] signals and then into the cable switch. This is set up so that by simply changing the automatic cable switch you may pass either time-of-flight or linear signals. All logic signals [E,S,M] are fed into an ORTEC 418A universal coincidence module used for gating of the linear signals. The AMP-SCA single channel analyzer output [E], which is the high bias requirement, must enter the "A" input of the coincidence unit which has an internal delay to bring the signal into time coincidence with the others [J,M]. The PSD [J] and low bias [M] logic signals enter the "B" and "C" inputs of the coincidence unit and a simple selection of switches on the front of this unit can select any combination of these requirements. One of the three linear signals [F,K,I] is then gated with the coincidence of the logic signals [N] in the ORTEC 442 linear gate and stretcher. The signal [P] is then ready to be fed into an analog-to-digital converter (ADC) for the computer. Note that the low bias level logic signal [C] does not actually come from the CFD but rather from the PSD module. This is simply a matter of convenience in making connections as the PSD box produces an output for every CFD output because the the CFD output is connected to the "strobe" input [B] of the PSD module and a PSD output is produced for every "strobe" input in the neutron+gamma mode.

Discrimination between neutron induced pulses and gamma induced pulses is set in the electronics by storing the linear output of the PSD-TAC in the computer gated by the PSD requirement and the bias requirement. As indicated in figure 2.10, the PSD requirement is then set above the gamma region (below the arrow in figure 2.10) yet low enough to include all of the neutrons(above the arrow). Generally the PSD is set with an Am-Be source because the charged particle beam impinging on the cell will produce so may gamma rays that the valley between the neutron peak and the gamma peak is not observable.

In actual data runs, the ratio of gamma rays to neutrons is about 10^4:1. During the actual experiment, most of these gamma rays are segregated without PSD by time-of-flight differences between neutrons and gamma rays. PSD windows are set to almost allow all of the neutron induced pulses in, even though it allows a fraction of the gamma induced pulses in. If a small fraction of the neutrons are not counted, it is compensated for since the fraction is the same over the entire time-of-flight spectrum so that the same fraction will be cut out for the normalization.

As has been mentioned, the system has the capability for bias setting in two different manners. These are referred to as 'high bias' and 'low bias.' The high bias setting is usually set at the Compton scattering edge of the 660 KeV

gamma ray from ^{137}Cs with the AMP-SCA. In these measurements, the low bias mode was used. Our low bias is at a minimum in the ^{241}Am gamma ray spectra indicated in figure 2.11. A simple algorithm has been established to ensure consistent setting of the bias relative to this feature of the spectrum. The low bias requirement is established through the bias setting on the CFD. Although the AMP-SCA provides a sharper cut-off, the CFD must be used to set the low bias because of dynamic range limitations (we require about 400:1) of the AMP-SCA and the more diffuse cut-off of the CFD is not a limitation. The ^{241}Am gamma ray is at 60 KeV which corresponds in pulse height in our detectors to a neutron energy of about 250 KeV. The reason for the difference in pulse height to energy ratios between gammas and neutrons again is due to the fact that gamma rays interact primarily with the electrons in the scintillator through electromagnetic interactions. Neutrons can only impart a substantial fraction of their energy to particles of nearly the same mass, therefore the principal light producing reaction is interactions with protons. Electrons and protons have different light producing characteristics in the scintillator. In principle, the bias check may be set up under computer control with the computer controlled cable switch and computer controlled sources in both the "4-meter" and "6-meter" detectors.

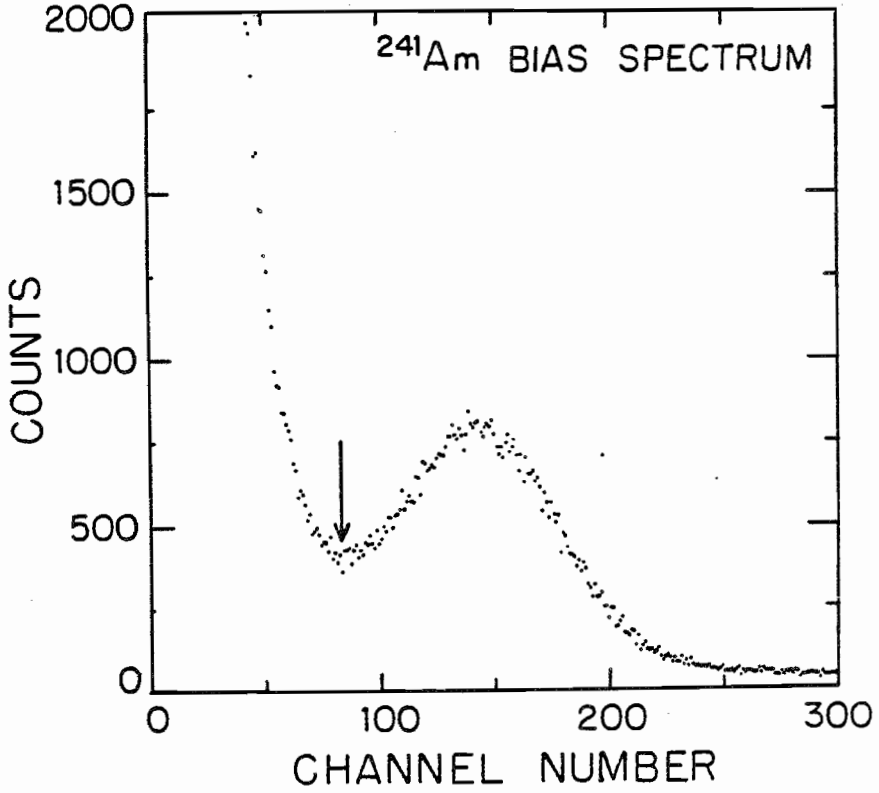

Figure 2.11 A sample ^{241}Am pulse-height spectrum used to set the detector "low bias" requirement. The bias point is shown by the arrow at the minimum which is a reproducible feature of the spectra.

III Data Reduction

Neutron angular distributions to the continuum were measured by taking data at 3 sets of angles with both detectors. Usually one overlap point was taken to ensure that both detectors were consistent with one another. Angles were alternated between detectors to aid in detection of systematic errors between the two detectors.

3.1 Data Acquisition Program

The data taking program is the same used by Glendinning[4]. This program has been rewritten to allow data acquisition with four detectors rather than the previous two detectors. It has the capability to handle all data taking functions, including control of ADC's and scalars. Simple on-line data analysis can be performed such as background fits and subtraction, window sums, generation of differences, and plots of the data. The code has certain control functions such as automatic termination of the runs by a best use of time algorithm for optimimum statistics[4]. Source-bias setup and sample moving may be performed by the program although these functions have not yet been used in experimental runs. Many functions are programmable into a master sequence,

reducing many switches to perform a set of functions into one switch.

3.2 Experimental Procedure

Generally four samples were measured together as a set, requiring the mounting of four samples and a blank wire on the string at one time. Measuring several samples at a time eliminates time spent on sample out measurements because one sample out-count can be used for each of the several sample in counts. For each element and each scattering angle, four spectra were required. Examples of these spectra are shown in figures 3.1,3.2,3.3. The four spectra at each energy were taken with (1) source gas in, scattering sample in, (2) source gas in, scattering sample out, (3) source gas out, scattering sample in, and (4) source gas out and sample out. In the case where the $T(p,n)^3He$ source reaction is used, for the gas out run, the cell is filled with ^4He gas at a pressure equal to that used for tritium for the 10- and 12-MeV cases for the purpose of a gas-out count. This was done to simulate stopping power effects for the incident protons. When the $D(d,n)^3He$ source is used, the gas out runs are taken with the cell at vacuum to avoid ^2D breakup that would occur on any inert gas. The reason four spectra are taken is as follows. The gas in spectra contains contributions of neutrons produced in the source gas as well as the cell

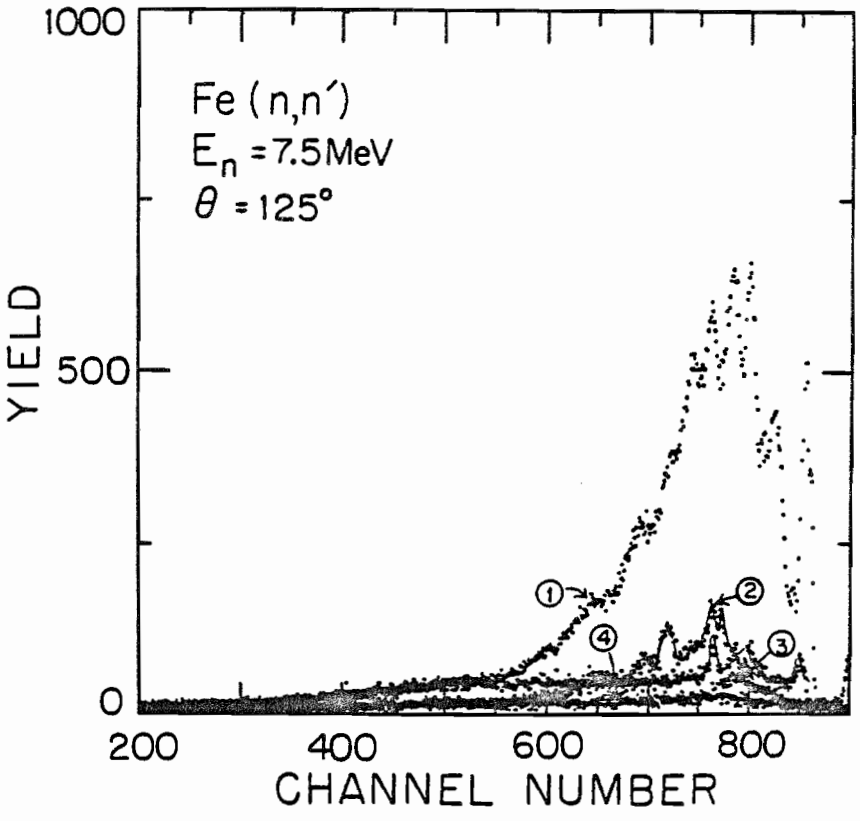

Figure 3.1 Four experimental spectra required for the measurement of one experimental angle at one energy for 7.5 Mev incident neutrons. The spectra are taken with (1) source gas in and scattering sample in, (2) source gas in and scattering sample out, (3) source gas out and scattering sample in, (4) source gas out and scattering sample out.

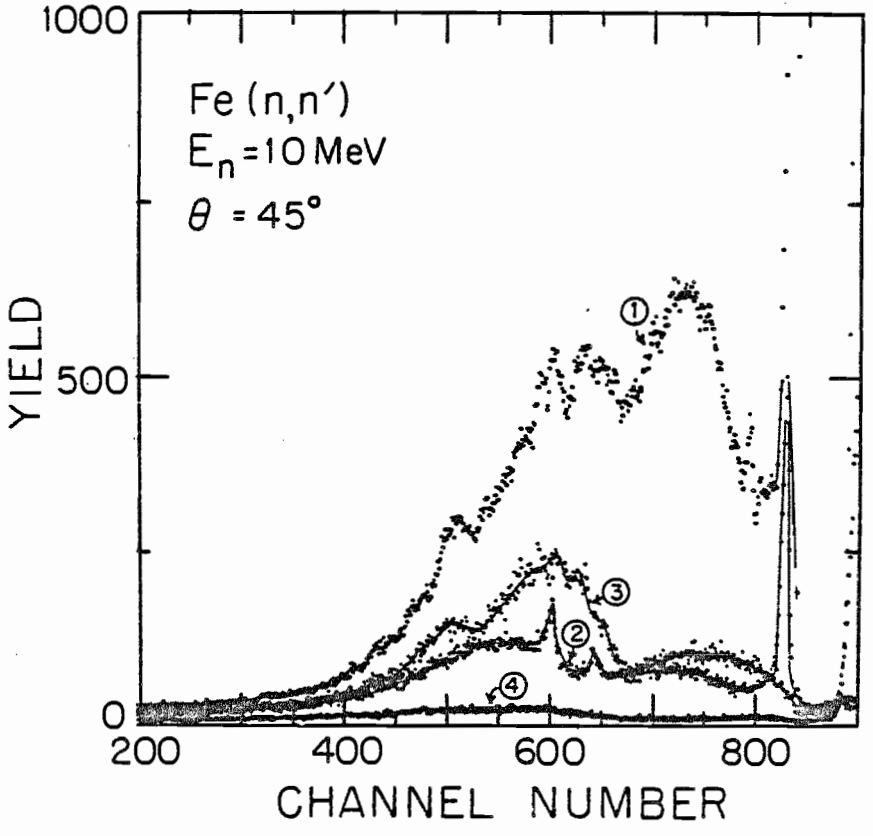

Figure 3.2 Same as figure 3.1 except for 10 MeV incident neutron energy.

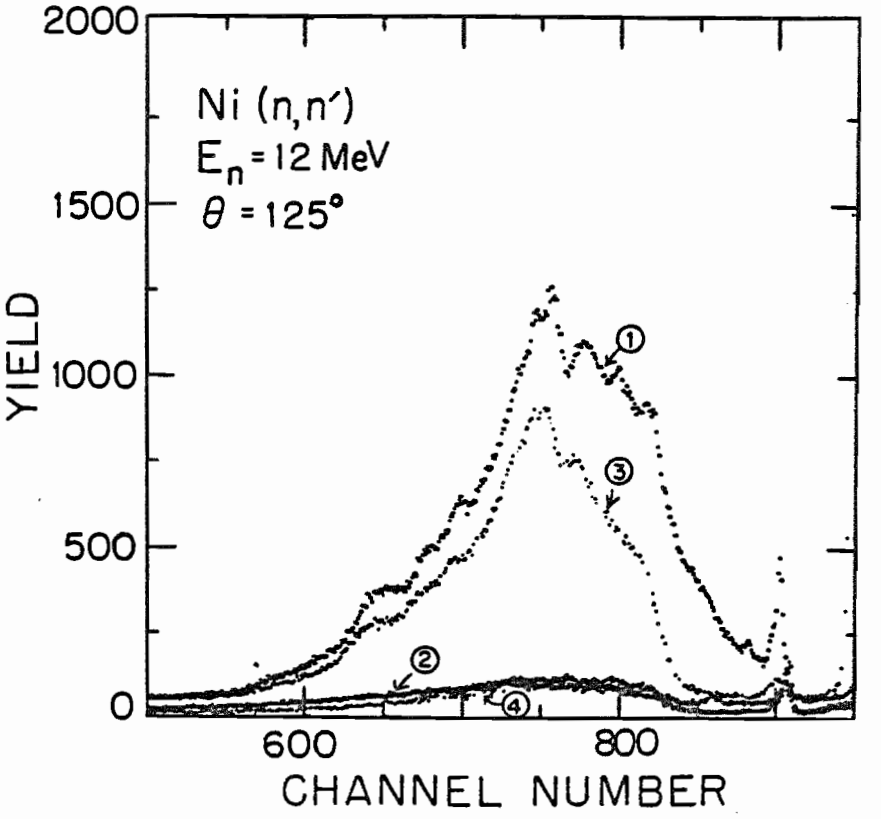

Figure 3.3 Same as figure 3.2 except for 12 MeV incident neutron energy.

walls. The gas out contains only those contribution from neutrons produced in the cell walls. The sample in spectra contain contributions from the sample as well as contributions from other things in the vicinity such as air, suspension apparatus, and shadow bars. The sample out contains only scattering from things other than the sample. The contributions in each of the 4 spectra has been expanded below illustrating the result yielded by the difference (figure 3.4). where P_g is the production of neutrons in the source gas, P_c is the production of neutrons on the cell itself. The scattering of neutrons from the sample is shown by S_s, and S_Σ is the scattering from things other than the sample as mentioned above. All spectra here are assumed to be properly normalized (see equation 3.1). The difference that results is an isolation of the neutrons produced by the gas (P_g) and scattered from the sample (S_s).

Typical run times are 3 hours for gas in, sample in, 2 hours for gas in, sample out. Gas out runs are typically 2 hours for sample in and 1.5 hours for sample out. These run times are not based on the optimization algorithm described by Glendinning[4]. The algorithm does not apply to the continuum measurements because the continuum distributions demand that a certain statistical accuracy be achieved over every portion of the distribution; an optimization of a sum over one region of the spectra is not good enough. Also the

configuration			contributions
	neut. source	scat. sample	
gas in, sample in	=>	(Pg+Pc)(Ss+Sx)	= PgSs+PcSs+PgSx+PcSx
-gas in, sample out	=>-	(Pg+Pc) (Sx)	= -PgSx-PcSx
-gas out, sample in	=>-	(Pc)(Ss+Sx)	= -PcSs -PcSx
+gas out, sample out	=>+	(Pc) (Sx)	= +PcSx
difference		(Pg) (Ss)	<= PgSs

Figure 3.4 Components of the difference.

optimization algorithm will not apply to an out count that is to be used for several in counts. Furthermore the algorithm depends on monitor counts. In these measurements integrated beam current is used for normalization and a running account of this is not kept by the computer. Therefore run times are based on experience of the statistical error contribution of each type of run to the final result once the data has been converted to fixed-width energy bins.

A difference of the four spectra is formed in the following manner.

diff = [(gas in, sample in - gas in, sample out) -
(gas out, sample in - gas out, sample out)]

Examples of these differences for the spectra shown in figures 3.1,3.2, and 3.3 are shown in figures 3.5 - 3.7.

The spectra in figures 3.1-3.3 and 3.5-3.7 are examples of those obtained for these cross section measurements. The elastic and first inelastic scattering peaks are the prominent peaks near the highest channels in each figure. The lowest channels contain few counts as they correspond to neutron-flight times below our detector bias. The central region contains the continuum scattered neutrons. In the 7.5 and 10 MeV data, there is a smaller peak up in the continuum which corresponds to a feature which appears in

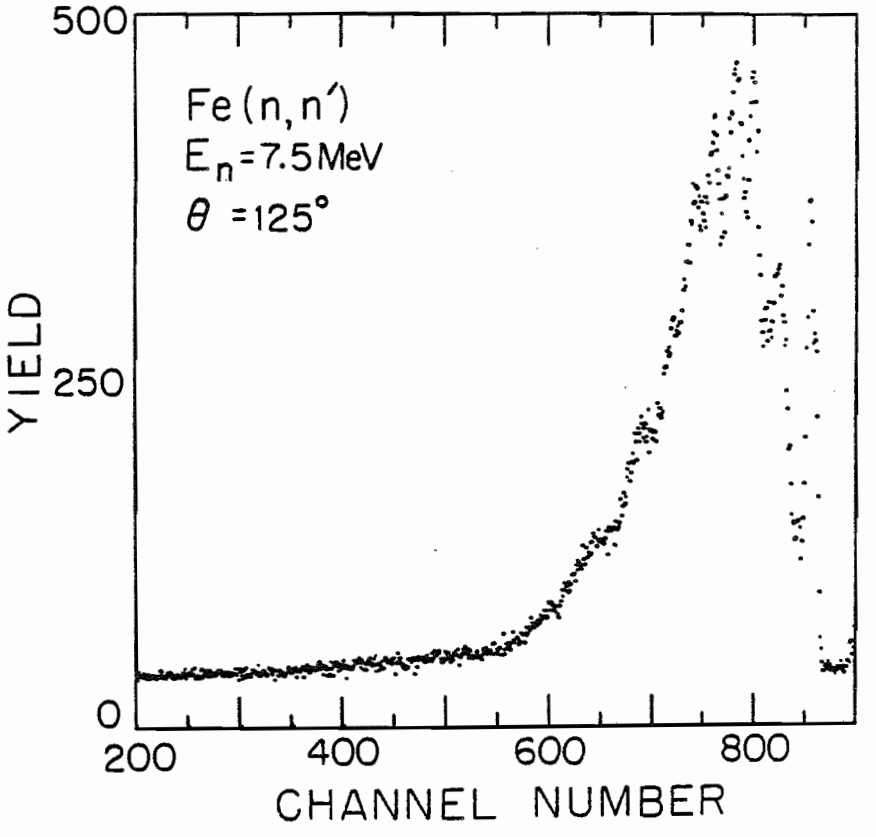

Figure 3.5 Example of a difference spectra for 7.5 Mev incident neutron energy. This spectrum has been formed in the manner of equation 3.1 (see page 46) with the data of figure 3.1.

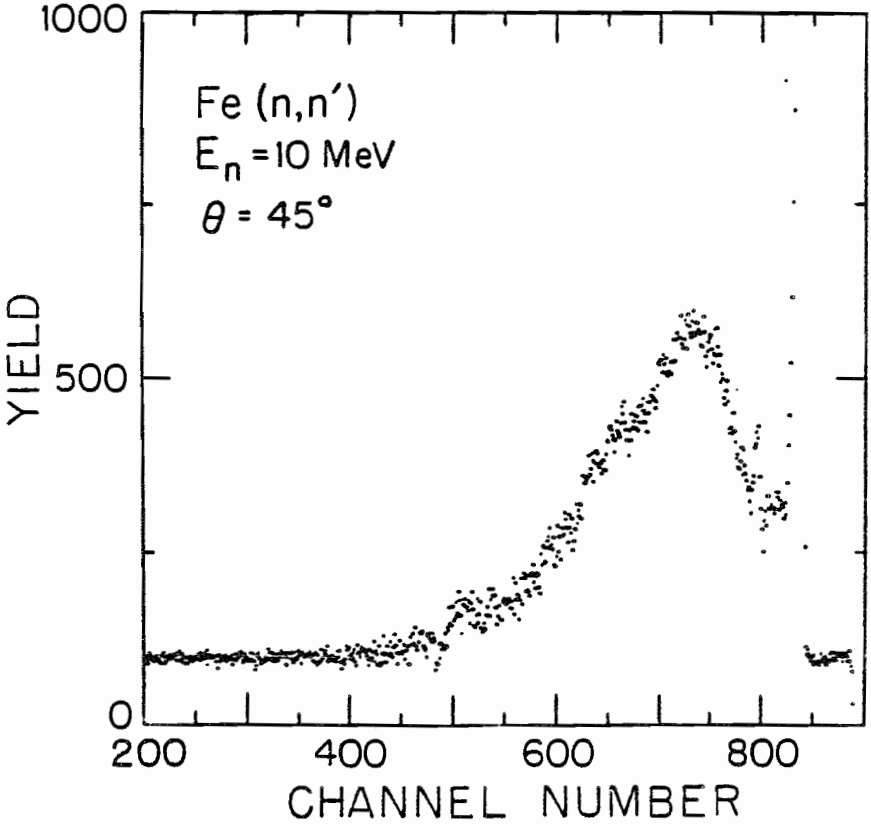

Figure 3.6 Example of a 10 MeV incident neutron energy difference spectrum formed in the same manner as figure 3.5.

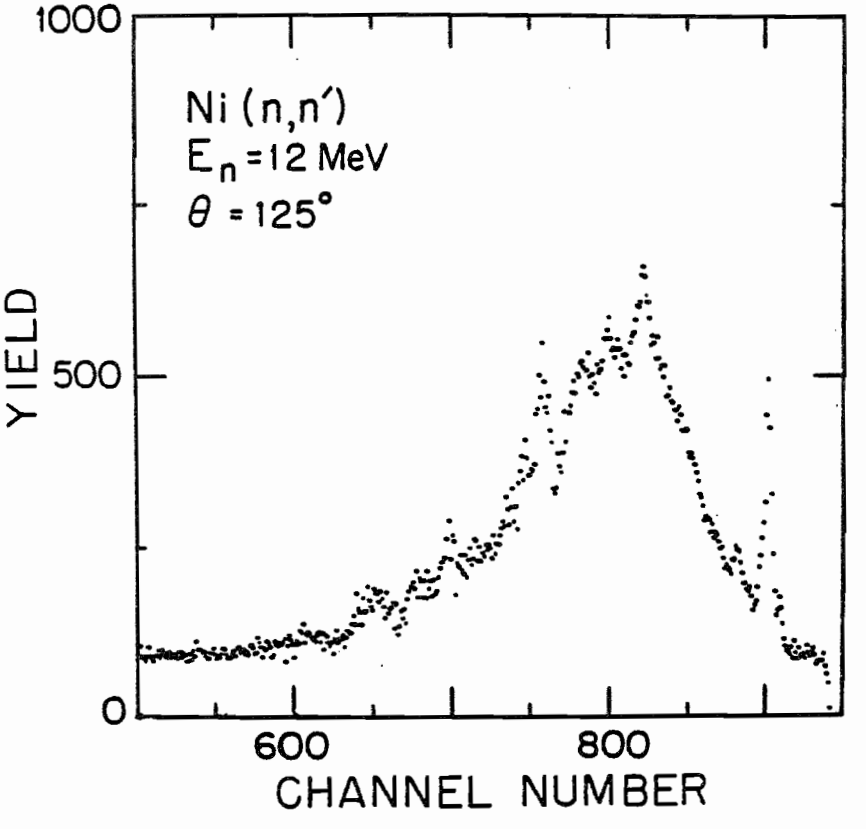

Figure 3.7 Example of a difference spectrum for 12 MeV incident neutron energy.

all of these spectra in both Ni and Fe at an excitation of about 4.5 to 5 MeV and has been previously observed, for example by Kinney and Perey[9]. At 7.5 MeV the difference (figure 3.5) resembles the gas in, sample in spectra (figure 3.1-[1]) because most of the contribution is from this spectra. Breakup neutrons are almost non-existent at these energies as evidenced by the small contributions from the gas-out spectra (figure 3.1-[3] and [4]). At 7.5 MeV structure appears at lower energies probably due to the increased energy resolution of the time-of-flight spectrometer for lower out-going neutron energies (the resolution varies proportional to $E^{3/2}$). This structure is similar to that observed by Kinney and Perey[9] in their work with Fe and by Rigoleur, Perey, and Kinney[23] in Ni. At 10 MeV, the structure is no longer observed, probably due to the much higher level densities at excitations where our resolution is good. The 10-MeV spectra (figures 3.2 and 3.6) is taken with the T(p,n) source reaction. Note that the gas-out spectra (figure 3.2-[3]) begins to be important, though most of the effect is at the very lowest energies. The difference (figure 3.6) results in a cancellation of most of the structure found in each of the individual spectra (figure 3.2). This is one of the better cases of this subtraction, although not atypical of the situation at 10 MeV. Subtractions at 10 MeV are generally much better than those at 12 MeV. Note that since this is a 45^{o}

spectrum the elastic peak has been truncated. The 12-MeV spectra (figures 3.3 and 3.7) show much more pronounced gas breakup problems (figure 3.3-[3]). At 12 MeV, neutrons produced by the cell itself are more numerous than those produced by the primary source reaction. The result of the subtraction is shown in figure 3.7. Much of the structure is left and is due to energy and timing drifts in the beam over the several hours between gas-in and gas-out runs made necessary by low count rates. A simple time shift has been found inadequate to correct these subtraction difficulties. This example shown in figure 3.7 is typical of the results obtained at 12 MeV. Note that resolution problems cause the continuum neutrons to smear under the elastic peak causing additional correction problems(see Chapter V).

During the course of the run, the anode signal pulse height bias setting is checked every time the detector angles are changed. Two scattering measurements are performed for polyethylene for each energy set for normalization purposes (which will be elaborated on later). Pulse-shape discrimination settings are checked at the beginning and end of each energy set.

3.3 Offline Procedures

A flowchart of all of the computer programs that the data passes through is shown in figure 3.8. Offline analysis of these data begins with the program TOFC. The TOFC code was written specifically for the analysis of continuum neutron scattering data. The program handles data for all four detectors for the 4 spectra taken for each detector. In addition to these 16 spectra, the code keeps differences between sample-in and sample-out for both gas-in and gas-out, as well as the final difference (as in equation 3.1). Also, energy spectra are kept for any one of the time-of-flight spectra. In addition, statistical uncertainties are kept for each data point of the above mentioned spectra. The spectra require about 50K words of computer memory exclusive of the coding and this is to be done on a 32K word computer. Therefore an offline storage system was developed on the drum to serve as a temporary storage for most of these spectra.

The TOFC code can handle all of the reduction of the data to "raw" cross section form. These raw cross sections have had all of the effects which can be experimentally accounted for removed but need further correction for experimentally unaccountable effects. These unaccountable effects will be elaborated upon in Chapter IV. First differences are formed

using the formula

$$3.1 \quad Diff = \left\{ \frac{(C^{in}_{in})}{(B^{in}_{in}\ 10^{-5}\ L^{in}_{in})} - \frac{(C^{in}_{out})}{(B^{in}_{out}\ 10^{-5}\ L^{in}_{out})} \right\}$$

$$- \left\{ \frac{(C^{out}_{in})}{(B^{out}_{in}\ 10^{-5}\ L^{out}_{in})} - \frac{(C^{out}_{out})}{(B^{out}_{out}\ 10^{-5}\ L^{out}_{out})} \right\}$$

$$+ BIAS$$

In equation 3.1 (C^{gas}_{sample}) etc. refers to counts obtained in the configuration with the gas situation noted in the superscript and the sample position noted by the subscript. B is the total charged particle beam charge collected during this run. It is used for normalization. L is the percentage of the time the computer was able to accept data and serves as a correction for dead time effects. L and B have the same subscript and superscript convention as C. No correction is made for non-computer electronics dead time or the effect on dead time of pulsed beam since the computer dead time is larger than these effects and is therefore the major contributor. BIAS is a constant added to every point to prevent over-subtraction leading to negative data points. (Such negative points cause practical difficulties with the program.) The factor of 10^5 is to prevent loss of precision in the integer storage of the quantities since the B's are of this order. In addition to the spectra, statistical

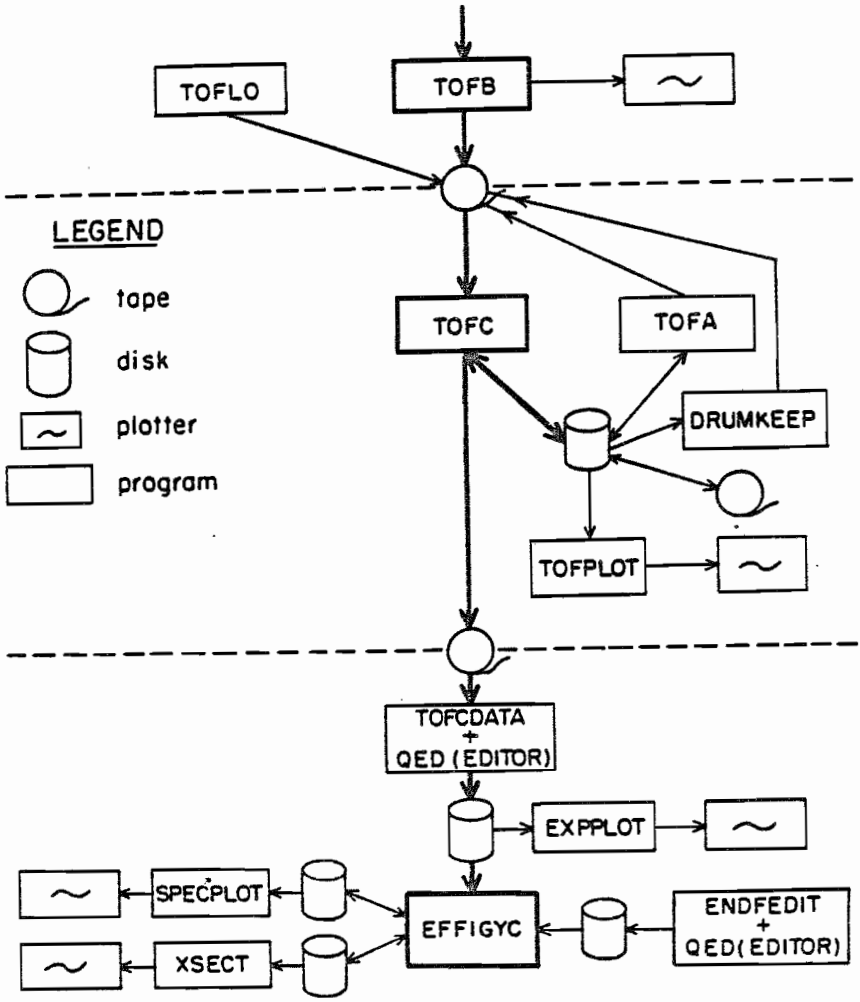

Figure 3.8 Flowchart of the computer programs used to process neutron scattering data.

errors are kept for every point, errors being added in quadrature. These errors include only counting statistics. Other sources of error such as normalization error, and data correction errors are evaluated separately. After subtraction of the four spectra, a flat background is fit to the data in the region above the source primary-neutron energy and the region below the experimental bias and subtracted. In these regions the only contributions are due to random events as there are no time correlated events which can appear. Most of this background is probably due to gamma rays scattered about the room as the gamma intensity exceeds the neutron intensity by orders of magnitude.

Time-of-flight spectra are converted to energy spectra in fixed-energy bins by summing all of the time-of-flight counts between energies corresponding to the bottom of the bin and the top of the bin. In other words the sum is carried out over all time-of-flight channels between NdE and (N+1)dE for the Nth energy bin, where dE is the width of an energy bin. This method has the advantage that the total number of counts in the spectra is preserved. Absolute time scale is determined by the arrival time of the gamma rays produced by neutrons in the scattering sample at the detector. This works with the D(d,n) reaction, however with the T(p,n) source reaction the gamma rays produced in the

cell and scattered by the sample overwhelm the gamma-rays produced by neutrons in the sample which are the gammas which establish zero time. Therefore the gamma arrival time must be adjusted slightly for T(p,n) source data so that the elastically scattered neutrons have the correct energy.

Detector efficiency is folded into the data during the time-of-flight to energy conversion by dividing each channel in the time-of-flight spectra by the efficiency at the mean energy of that time channel. The detector efficiency curve is shown in figure 3.9. Since our correction code uses the time-of-flight spectra the energy spectra are not used for final data but they serve as a very useful preview at the data since correction is mostly a matter of scale. Also, as will be discussed later, the data can be divided by the energy of the outgoing neutron and plotted on a log scale, which should yield a straight line as a function of energy whose slope will be the nuclear temperature. All spectra are dumped onto the drum where they can be saved, and then compressed from 1024 channels to fit into 256 channels to allow the correction program to handle it. Compressed spectra are then sent to the TUCC computation center for correction.

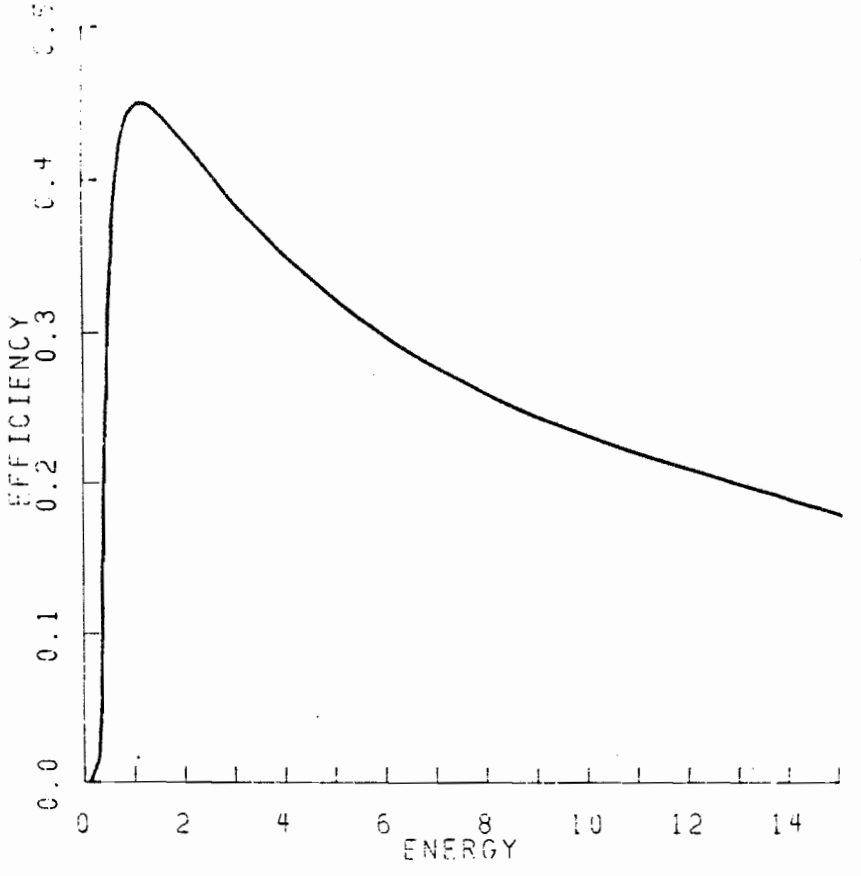

Figure 3.9 **Detector efficiency at low bias.**

3.4 Normalization

These data have been normalized to absolute cross section through comparison of measured count rates to count rates measured for a polyethylene sample and the known hydrogen cross section[24]. The count rate in the sample of iron or nickel is related to the count rate of the polyethylene sample by the relation expressed in equation 3.2.

$$3.2 \qquad \frac{N_s(E)}{\frac{d\sigma_s}{d\Omega}\,\eta(E)\,n_s} = \frac{N_{poly}(E_{poly})}{\frac{d\sigma_{poly}}{d\Omega}\,\eta(E_{poly})\,n_{poly}}$$

This can be solved for $d\sigma_s/d\Omega$ and all other quantities are measured for each run. At least twice for each energy, a polyethylene spectrum and a carbon out count spectrum are taken. The difference between the polyethylene spectrum and the carbon spectrum (the carbon sample contains the same number of carbon atoms as the polyethylene sample) yields the count rate for only the hydrogen atoms in the polyethylene sample. The difference is formed in the same manner as for the unknown scattering samples as in equation 3.1. The difference spectrum shows only a peak which is

summed to form the hydrogen scattering yield. This yield is corrected by the computer code EFFIGY as for any two element sample. This work has been carried out by El-Kadi and Glendinning and is described by El-Kadi[5]. Typical hydrogen yield correction factors are 15-20%. The empirical relation of Glasgow[20] relating the heights and diameters of scattering and normalization samples has been abandoned in favor of larger polyethylene samples resulting in less time for normalization samples and the need for these corrections which have not been applied to previous TUNL data. Care is taken to locate the hydrogen peak as far as is possible from the carbon elastic and carbon inelastic peaks by choice of scattering angle, usually 32-35°. Detector efficiencies are measured in separate experiments as previously mentioned. The number of atoms in each sample is determined by careful weighing and knowledge of the weight of the individual sample molecules (polyethylene is assumed to have a composition of $n(CH_2)$). The normalization factor $(d\sigma_s/d\Omega)/N_s$ is applied to the time-of-flight spectra to yield double differential cross section in $d\sigma/d(\text{channel})\, d\Omega$. EFFIGYC accepts these time-of-flight spectra in macroscopic cross section units (cm^{-1}) which is obtained by multiplying the microscopic cross sections by the sample density.

IV Data Correction

4.1 Need for Data Correction

The experimental configuration for these experiments, shown in figure 4.1, requires the sacrifice of ideal experimental geometry in order to obtain reasonable count rates. We accept the need for large corrections to these data, brought about by the geometrical compromises, in order to obtain better counting statistics. In addition, since the source of neutrons is not mono-energetic, corrections for the undesirable source neutrons must be made. The compromises are required due to four basic reasons. 1.) These experiments measure events which are a result of a double process since a source reaction must first produce the neutrons and then the neutrons must be scattered before detection. 2.) Since the charged particle beam must be pulsed, a substantial fraction of the beam is lost in the pulsing process. This problem is more severe in these measurements than some others conducted at TUNL because the detection of the low energy neutrons requires long times between pulses. 3.) Time-of-flight spectrometry requires long sample to detector distances. Energy resolution is proportional to the flight path but count rate is inversely

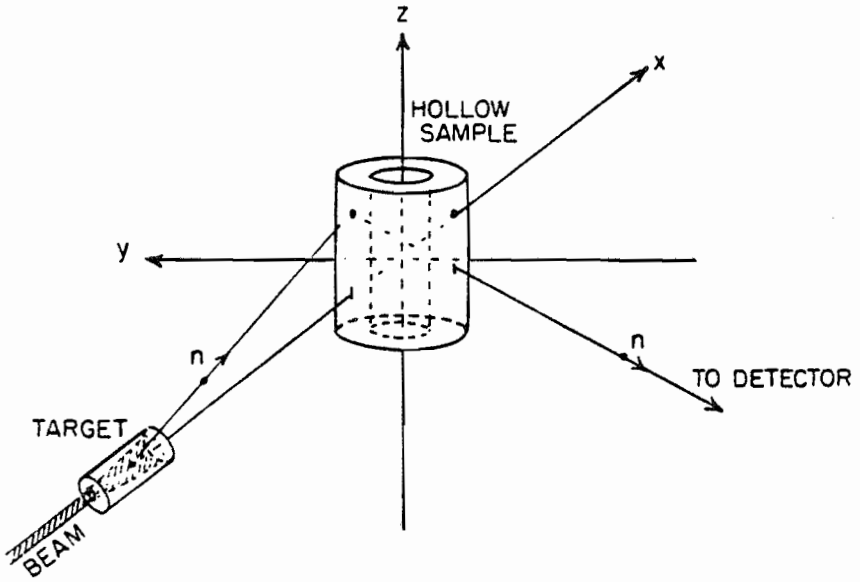

Figure 4.1 Geometry of gas cell, scattering sample, and detectors.

proportional to the square of the sample-to-detector distance. 4.) Both the neutron production cross sections and the neutron scattering cross sections are not particularly high. Since our experiments already require about 12 hours per angle for a given incident neutron energy, it is not possible to approach an ideal geometry.

To increase the counting rate, three geometrical compromises have been made. The neutron source has been extended. Our neutrons are produced in a cylindrical active gas volume approximately three centimeters long and one millimeter in radius. Secondly, large samples are used. This means the entire sample cannot be located at zero degrees but rather must subtend a finite solid angle. These samples are large enough for screening effects to be important. Further count rate increases are obtained by locating the sample near the neutron source, since the count rate is also proportional to the inverse of the square of the source-to-sample distance. This means, with the large source and sample, that there is a relatively large range of source-to-sample distances.

The effects of these geometric compromises, experimentally unsubtractable gas-breakup neutrons, finite time and energy resolution, and the interaction of these effects require correction. The effects are not independent

of each other. The interactions of these effects can be important and are therefore all calculated simultaneously. There are four principal geometric effects. 1.) There are angular resolution effects due to the angular spreads of the scattering sample as it views the source and of the detector as it views the sample. For portions of the elastic scattering distribution, the average scattering angle may be as much as four degrees different than the geometric scattering angle, depending on the anisotropy of the angular distributions. 2.) The large range of source-to-sample distances can cause difference between the average source-to-sample or sample-to-detector distances and the geometric mean distances. This effect is most pronounced in the source-to-sample distance and is typically slightly less than a 10% effect due primarily to flux differences in the different parts of the sample. 3.) Energy resolution effects can also be important due to both charged particle energy loss in the gas cell and kinematic energy differences due to angular differences of emitted neutrons. 4.) Attenuation effects which are discussed in the next paragraph.

With large scattering samples, the effect of attenuation is important. For the purposes of the computation, attenuation is defined as the effects processes which remove valid events from detection. This includes only "out-

scattering" processes, so that once an event has been attenuated out of the flux, it is assumed it will never reach the detector. Those that are rescattered into the detector or were initially headed in the wrong direction but are "out-scattered" into the detector are accounted for under the heading of multiply scattered events. Our large samples have an overall source-to-detector attenuation of about 30%, with roughly half of this due to average source-to-sample attenuation and half due to sample-to-detector attenuation. These figures are arrived at through experience with EFFIGYC calculations for these samples. Here source-to-detector attenuation refers to the attenuation suffered by the average neutron in its path from source to detector. Attenuation effects are mostly a scale factor to this data. In addition to attenuation effects, which cause a loss of neutron flux, there is a multiple scattering effect or "in-scattering" effects. Since a neutron which has been scattered out of the primary flux (attenuated for example) may still reach the detector by scattering again, we must account for these multiply scattered neutrons. In the continuum region, multiply scattered neutrons almost make up for most of those lost due to attenuation, but in the higher energy discrete region the multiple scattering adds back only about 10% of the neutrons as compared to 30% lost due to attenuation in some regions. These percentages are obtained from experience with EFFIGYC.

Source gas breakup neutrons also must be accounted for. These lower energy neutrons can interact in all the ways the primary source neutrons can, but are not part of the effect we wish to measure. These gas breakups range from a negligible fraction of the primary strength at 7.5 MeV to 16% at 12 MeV. As has been mentioned, these cross sections are the result of the work of Drosg et. al.[18] This ratio has been shown in figure 3.4

4.2 Approach to the Problem

Since these effects are complicated and tedious to account for, a computer has been used to find a solution. By means of the code EFFIGYC all of these effects are accounted for simultaneously. Through simulation of experimental spectra we can iterate to cross section which best produces the experimental result. Details of the simulation and iteration processes are discussed in section 4.5.

EFFIGYC is based on a similiar code written to correct discrete scattering data called EFFIGY. The work which resulted in the Effigy codes is based on earlier work by Cox[25], Kinney[26], and Velkley, et. al.[27] in correction of neutron scattering data. The general procedure used to solve these problems is outlined in figure 4.2.

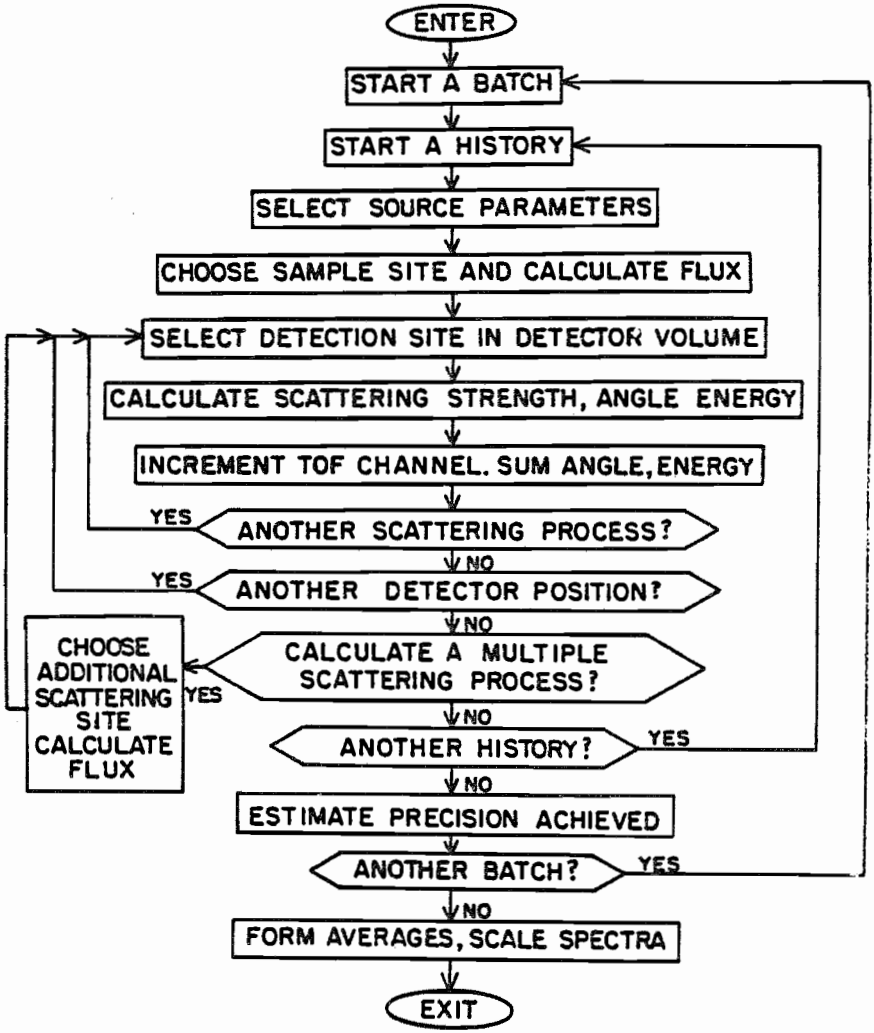

Figure 4.2 Flowchart for the simulation and correction of this scattering data.

4.3 Features of EFFIGYC

The EFFIGYC code has many data requirements. In order to simulate the experimental result, the code needs cross section data for scattering, source cross section data, geometric data, experimental data, and program flow control parameters. (A more complete description of the EFFIGY codes, including data requirements, operation detail, and simulation procedures can be found in the documentation for the program[28], while a summary of this information has been reported by Hogue and Beyerle[29].)

Scattering cross section data includes total cross section data used to calculate attenuation effects and to calculate losses to other channels for multiple scattering purposes. Cross sections for all discrete states to be considered must be included for all possible incident neutron energies and neutron exit angles. Continuum scattering cross sections must be specified for all incident and exit neutron energies as well as angular distribution data. The continuum cross sections are the only ones that are adjusted. Cross section estimated must be given for all energies which are possible to reach under the experimental conditions for each of the above.

Source cross sections must also be specified. Incident energy and angular distributions of emitted neutrons must be given to allow calculation of source anisotrophy effects for primary neutrons. Source breakup distributions must be specified as a function of exit neutron energy.

Properties of the experimental set-up are required. These include geometric properties of the experiment, detector efficiency, and information about the beam and sample properties.

Experimental time-of-flight data must be input for comparison with calculation to allow adjustment of cross sections. These are the difference spectra such as those shown in figures 3.5-3.7.

Control of the flow of the program is carried out through certain control keywords. Figure 4.3 illustrates the method of control of program flow through these keywords, as well as listing all input data and control words. Note that the sequence of the calculation is determined by the user rather than being predetermined, thus offering greater flexibility. The EFFIGYC code has been written to carry out the complex task of correction of this data yet be relatively easy to use. In addition EFFIGYC has several unique features.

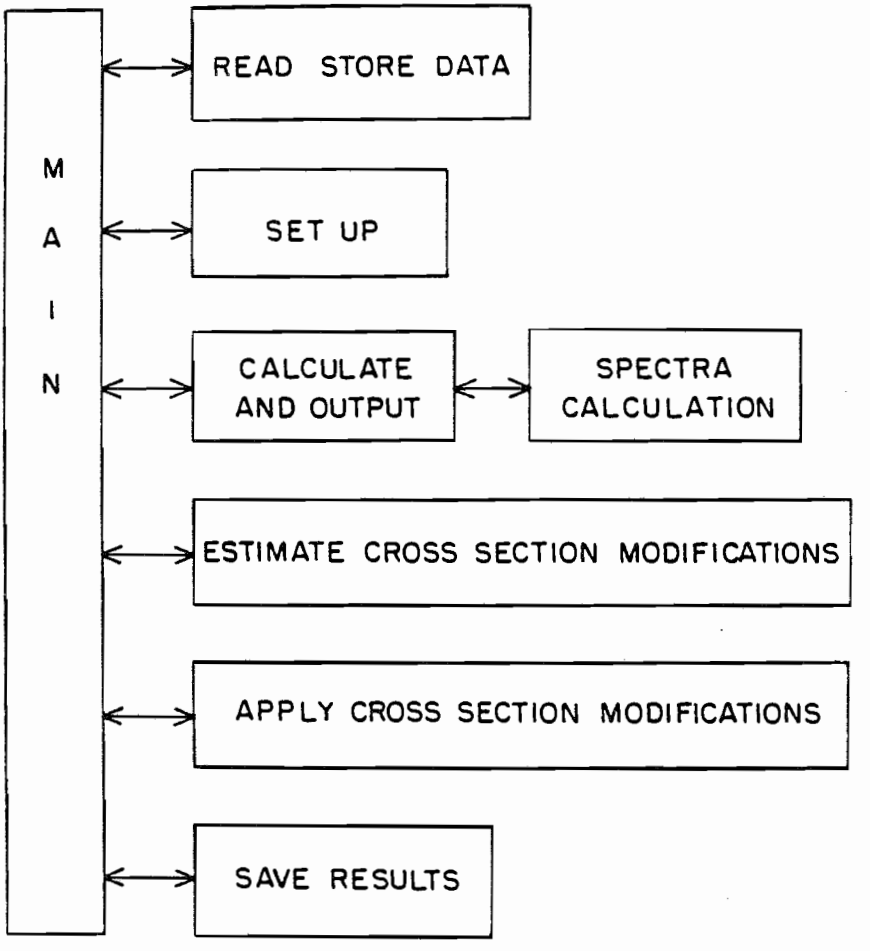

Figure 4.3 Input scheme for EFFIGYC.

EFFIGYC is half of a pair of programs which use similar simulation techniques. This facilitates the verification of the EFFIGYC code since there is no code to which we can compare the results of EFFIGYC, but we can compare most of the features of EFFIGY (the other code) to other codes. The writing of EFFIGY was carried out by H. Hogue[3]. Since the two codes can calculate most of the same effects, it is useful to carry out comparisons of the two for verification purposes.

The continuum measurments require simulation of gas breakup effects. These gas breakup effects interact with other effects in a complicated way. EFFIGYC has the unique feature of a simulation of these effects in the same way as it accounts for the primary source neutrons.

The continuum scattering cannot be accounted for independent of discrete scattering. EFFIGYC simulates continuum scattering using the same coding as for discrete events. Not only will discrete states affect data in the continuum region but certain states in the continuum region may be enhanced over the smooth continuum. EFFIGYC allows superposition of discrete strength in the continuum region to account for energy structure.

EFFIGYC includes realistic simulation of time-of-flight spectra based on system parameters. This allows the inclusion of rather complicated smearing effects brought on by finite time and energy resolution, and finite geometry effects. This allows direct comparison with time-of-flight spectra. EFFIGYC has been written to be portable. Standard Fortran has been used throughout. The only change that should be required for moving the code is the inclusion of a random number generator.

This code requires considerable computer resources. Time savings have been given priority over space resources where such trade-offs exist. Space requirements are about 550K bytes at four bytes per single precision word. This data requires about one hour of IBM 370 CPU time per detector per energy per element for final corrections.

4.4 Method

The averaging over the many effects on the cross section measurement is expressed by the integral operator for the averages F.

4.1 $$\sigma_{obs} = F(\sigma)$$

Ideally, we would like to invert this operator to the form

4.2 $$\sigma = F^{-1}(\sigma_{obs})$$

but this results in integral expressions which are very difficult to invert. In fact, even the integral expressions in equation 4.1 make it difficult to solve by analytic methods. Not only are the integrands difficult to write in a functional form but the limits of integration are difficult to specify in some cases as they are complicated functions of many lower order variables. We chose to solve this integral using a Monte Carlo technique and adjust the integrand iteratively until we can reproduce the observed cross section (σ_{obs}.)

The Monte Carlo technique involves sampling the integral many times to obtain an evaluation of the integral. This is a very physical approach for the computational problems of

these kinds of experiments. The experiment samples the observed effect by measuring many neutrons which have a variety of different histories from source to detector. One important difference between the Effigy codes and nature is that interactions in the code are forced and then weighted rather than allowed with their natural freqnencies. In nature each event is of course allowed to occur with its natural frequency and each is given equal weight. The main result of this difference between experiment and calculation is a saving of computer time and a difference in the error associated with each count rate.

The transformation between a continuous integral and a discrete numerical solution will involve transformations between coordinate space and "test point" space of the form

$$4.3 \qquad F = \int_x f(x)\, dx = \frac{1}{di/dx} \sum_{i-1}^{N} f_i\, di$$

so that the integral over infinitesimal coordinate differentials is approximated by a sampling of the integrand at many test points of the coordinate being evaluated[30,31,32]. f_i is the set of weights appropriate to the calculational history i, di/dx is the Jacobian for the transformation. Note that the distribution of test points (di/dx) must be a constant for this to be allowed. For

be chosen uniformly in volume V to allow equation 4.3. In this case di/dx = N/V.

4.5 Solution of the Multiple Scattering Problem

The implementation of the solution of the functional F is through the simulation of the experiment in a physical sense rather than a mathematical one. It is easier to think about the problem in terms of modeling an experiment than the solution to an integral equation. However, to ensure that the modeling is done properly, the integral must be written down and reduced to discrete summation. The observed rate of scattering (R) can be expressed as

$$4.4.a) \quad R = \frac{\int_{E_{in}} \int_{V_s} \int_{E_1} \sigma_s(\theta_{out}, E_{in}(\bar{r}_s), E_1)\, dV_s\, dE_{in}(\bar{r}_s)\, dE_1}{\int_{V_s} dV_s \int_{E_{in}} dE_{in}(\bar{r}_s) \int_{E_1} dE_1\, \sigma_s(0^\circ, \langle E_{in} \rangle, \langle E_1 \rangle)}$$

b) $$\times \int_t S(t;E)\,dt \quad \frac{|\langle \bar{r}_s \rangle - \langle \bar{r}_1 \rangle|^2}{|\bar{r}_s - \bar{r}_1|^2}$$

c) $$\times \sum_i R_i(\bar{r}_s, \bar{r}_1, \ldots, \bar{r}_i, \bar{r}_d, E_{in}, E_1, \ldots, E_i)$$

d) $$\times \frac{\eta(E_d) \int_{V_{det}} \frac{1}{|\bar{r}_{out} - \bar{r}_{det}|^2}\, dV_d}{\frac{\langle V_{det} \rangle}{|\langle \bar{r}_{out} \rangle - \langle \bar{r}_{det} \rangle|^2}} ,$$

where σ_s is the source cross section energy and angular distribution, $S(t;E)$ is the incident beam resolution function, $|\bar{r}_s - \bar{r}_1|$ is the source point to sample point distance, $\langle\ \rangle$ denotes the mean of the enclosed quantity, R_i is the scattering rate for a process involving i interactions in the sample, $\eta(E_d)$ is the efficiency of the detector, E_{in}, E_1, ..., E_i are incident energies for the subscript order process with E_{in} being beam incident energy.

The equation is broken into four parts (a-d) for the purpose of this discussion. In every case, each integral

must be evaluated considering all dependent variables in the entire expression, with the groupings being for convenience of notation only. Part a) describes effects having to do with the source reaction. The integrals in line a) account for source finite geometry effects. The integral in the numerator expresses the weights for the source cross section. Since experimental normalization is carried out relative to the mean source cross section at zero degrees, the calculation must do the same thing. The denominator in line a) accounts for this relative normalization by dividing out this source cross section for mean source parameters.

Line b) of equation 4.4 shows the beam dispersion in energy and time and the flux weighting of the source. Again experimental normalization is carried out as though the geometric mean source-to-sample distance were the effective source-to-sample distance, so the correction for this normalization is included. S(t;E), the incident beam resolution function, involves a dispersive influence on the time-of-flight spectra due to finite beam pulse width and in energy due to beam energy spreads incident on the gas cell. Other time and energy spreads are introduced implicitly; for example, those due to kinematic energy-spreads implicit in angular averaging, differences in flight paths, or multiple scattering energy losses.

Line c) shows the contribution of scattering of source neutrons in the sample. The rate of scattering from the sample is a function of the location of all interaction sites and energies. The simplest interaction is a single interaction in the sample, but higher order processes must be taken into account. This requires summation of R for all orders of processes that contribute. This sum is infinite in principle; however only the first few terms contribute significantly. The code can calculate to any order but in practice it rarely choses to calculate beyond fourth order processes. Details of the function R and its reduction to a useful quantity in terms of scattering weights is shown in appendix A.

The last line of equation 4.4 (d) is the correction for the average over finite detector size. Here the experimental data normalization is carried out for a point detector so this must be accounted for. Detector efficiency is folded in at this point.

In order to evaluate these integrals by the previously described method, equation 4.4 must be transformed as in

equation 4.3 as follows

$$4.5 \quad R = \frac{| \langle \bar{r}_s \rangle - \langle \bar{r}_1 \rangle |^2}{\sigma_s(0^o, \langle E_{in} \rangle, \langle E_1 \rangle)} \times \frac{V_{samp}}{N}$$

$$\times \sum_{i=1}^{N} \frac{\sigma_s(\theta_{out}, E_{in}(\bar{r}_s)) + \{\sigma_s^{bu}(E_{in}^i, E_1^i)\}}{\{\sigma^{total}\}} \Big/ | \bar{r}_s^i - \bar{r}_1^i |^2$$

$$\times \sum_{j=1} \prod_{k=1}^{j} \rho \frac{d\sigma_{k,k+1}^i}{d\Omega} T_{k,k+1}^i 4\pi R_c \frac{\sum_{m=1}^{n} \sigma_m T_{j,d}^i}{\sigma_{total}}$$

$$\times \frac{\eta(E_{det}^i)}{| r_{out}^i - r_{det}^i |^2}$$

Where symbols remain as defined in equation 4.4 and Appendix A and are listed in the symbol table. Note that the sum over j is infinite in principle, but the code terminates the sum by virtue of the point selection process. The superscripts denote the evaluation of the quantity for a particular test point or "test event".

4.6 Iteration of Cross Section

Once the experimental result has been simulated, the cross section data must be adjusted so that they agree with the experimetal result. EFFIGYC does this by adjusting the continuum cross sections. Equation 4.1 expresses the relation between the single nucleon cross section (σ) and the cross section we expect to observe (σ_{obs}). Since we do not know σ but must make a reasonable estimate (otherwise there would be no point to these measurements), we cannot expect to simulate the experimental result precisely the first time. In practice, we have an expression for the situation after the first pass.

$$\sigma_{obs} = F(\sigma_{est}) + \Delta\sigma \qquad 4.6$$

Where $\Delta\sigma$ is simply the difference between the simulated result and the observed cross section. To correct for this difference the simple assumption is made that the discrepancy is due only to an error in the estimated cross section which has no effect on the corrections. This is of course a simplification but should be a step in the right direction. This assumption is expressed below.

$$F(\sigma_{est}) + \Delta\sigma = F(\sigma_{est} + \Delta\sigma) \qquad 4.7$$

This assumption need not be justified explicitly as it has

been shown to yield convergence, and once the condition

$$\sigma_{obs} = F(\sigma_{est})$$

is met, is assumed that $\sigma_{est} = \sigma$ since $F(\sigma) = F(\sigma_{est})$. In practical terms this means the difference between simulation and experiment is scaled by the calculated effect on the cross section and this is added to the estimated cross section to yield a new estimate of cross section

4.8 $$\sigma_{new} = F(\sigma_{est}) + \sigma_{est} \frac{\Delta\sigma}{F(\sigma_{est})}$$

for each time-of-flight channel. This procedure is repeated until convergence between experiment and simulation are achieved. Convergence is typically obtained after the 2nd attempt. Examples of some two-pass spectra are shown in figures 4.4-4.6 showing several of the calculated components as well as the experimental spectra. Note that there is no gas-breakup spectra in the 7.5 MeV spectra as this energy is below breakup threshold, but at 12 MeV the gas-breakup effect is as large as the effect we want to measure at certain points in the spectra. This is a principal factor in making these experiments difficult.

Figure 4.4 Time-of-flight spectra for simulation calculation after two iterations at neutron energy of 7.5 MeV. Spectrum 1) is the experimental spectra as in figure 3.5 compressed into 256 channels. Spectrum 2) is the simulation of this experimental spectra. Spectrum 3) is that part of the scattering involving single scattering of primary source neutrons. The ratio of spectrum 2 to spectrum 3 is a measure of the correction factor on the data excluding attenuation.

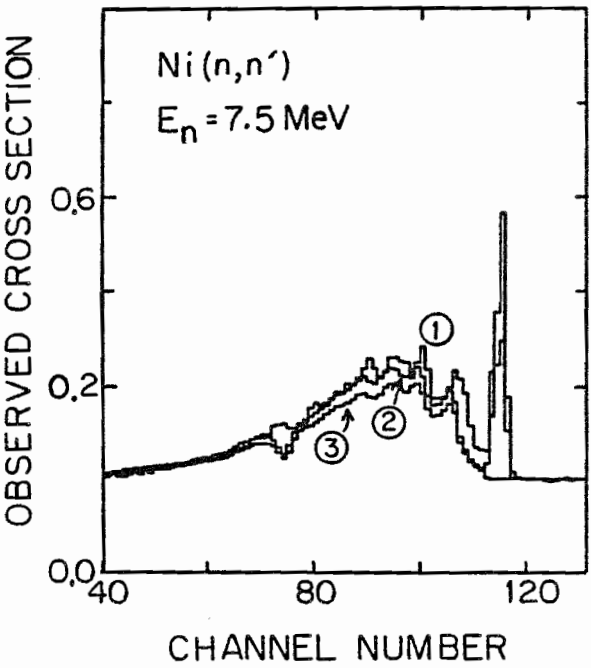
Ni (n,n′)
E_n = 7.5 MeV
OBSERVED CROSS SECTION
0.0
0.2
0.6
40
80
120
CHANNEL NUMBER
①
②
③

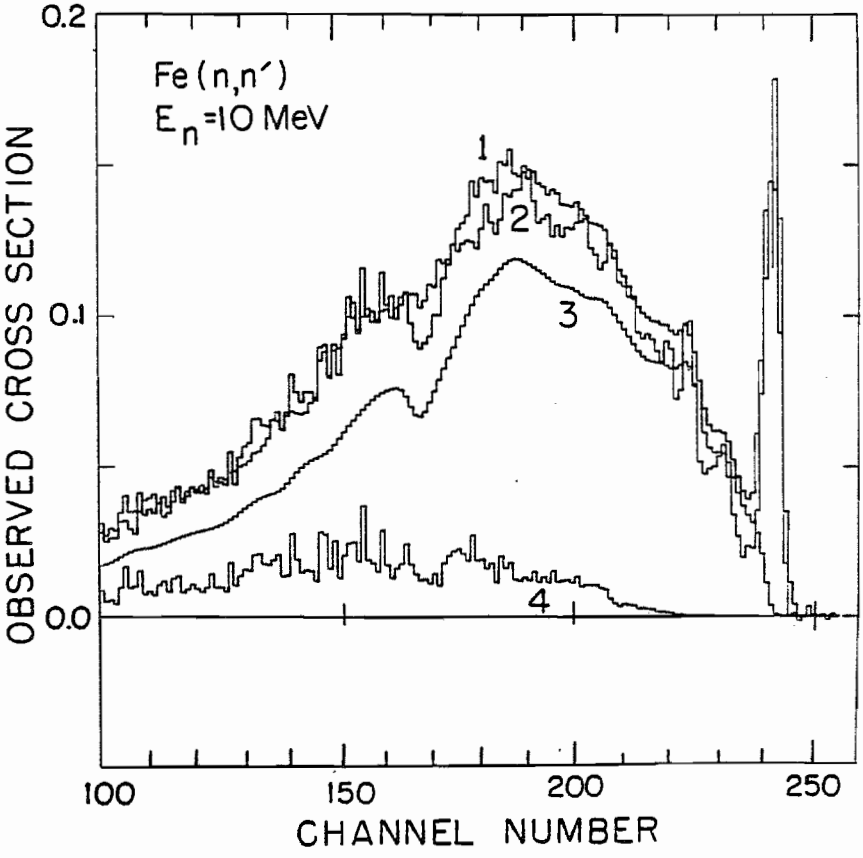

Figure 4.5 Time-of-flight spectra for simulation calculation at neutron energy of 10 MeV. Spectra are the same as figure 4.4 with 4) added which is the calculated scattering of all source gas-breakup neutrons.

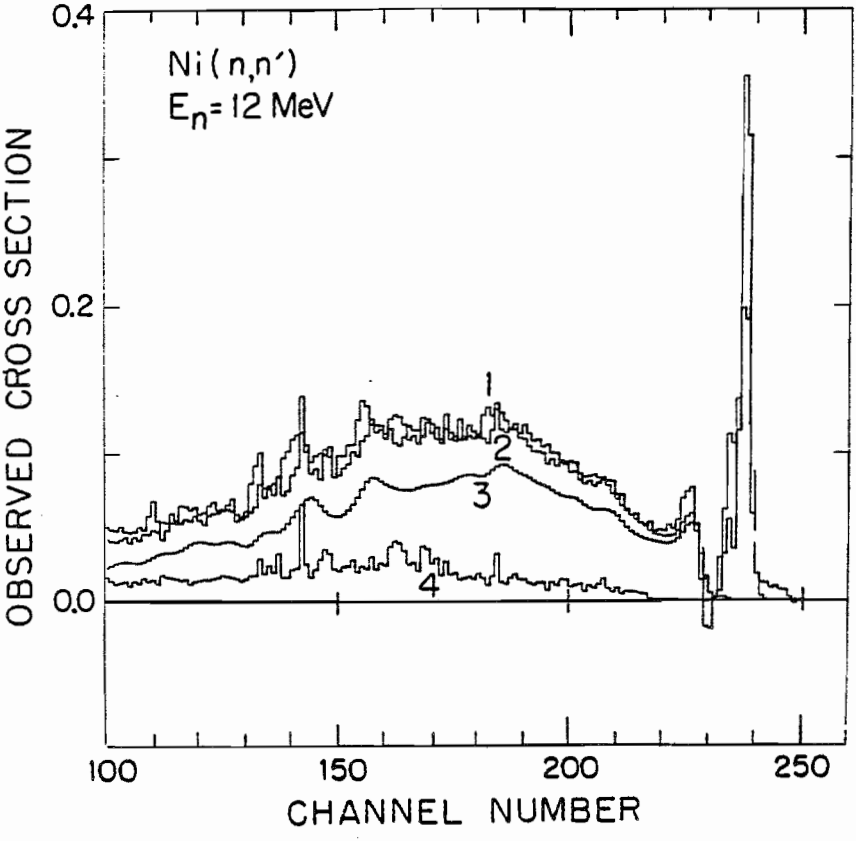

Figure 4.6 Time-of-flight spectra for simulation calculation at neutron energy of 12 MeV. Spectra are the same as figure 4.5.

V Analysis and Results

5.1 The Energy Distribution

Inelastic scattering to highly excited states in the residual nucleus serve as a test of the statistical model of the nucleus. In this model, the decay of the compound nucleus (the nucleus formed by the target plus a neutron) is treated independent of its formation. The scattering cross section is then simply expressed as

$$\sigma(E_n, E_{out}, \theta) = \sigma_c(E_n)\ P_d(E_n, E_{out}, \theta)$$

where σ_c is the cross section for formation of the compound nucleus, P_d is the probability of decay of the compound nucleus into one exit channel with exit neutron energy E_{out}. With this very simple parameterization, the overall features of the data are characterized quite well.

In this model, the assumption is made that the incident neutron shares its energy with all of the nucleons in the compound nucleus after it enters. The incident neutron which enters the target nucleus is very likely to undergo energy sharing interactions as it crosses the nucleus (the

mean free path of a nucleon of about $.4 \times 10^{-15}$ meters[33] is about 1/20 of the nuclear diameter of these target nuclei). Once the incident neutron has shared its energy with other nucleons in the system, it has a small probability of escaping the compound system because it lacks sufficient energy to escape. Since the incident neutron remains in the compound system for a long time (relative to the transit time of an unimpeded neutron across the nucleus), it is assumed that enough interactions occur for the system to reach equilibrium. The large number of interactions during the existence of the equilibrium compound system results in the loss of detailed information about the way it was produced. The information which persists is that about total energy, angular momentum, and parity of the system. This results in a system with a classical behavior. The interference terms, usually important in nuclear interactions, do not contribute in this case. This is due to the large number of levels in the compound and residual systems leading to experimentally indistinguishable processes, and the relatively large spread in decay times. Even the fact that there are discrete levels becomes unimportant as they are unresolvable. The system is analogous to evaporation from a liquid drop or radiation from a black body with the important difference that an "evaporation" of a single nucleon can result in a large "temperature" change of the system due to the substantial energy loss[34].

The formation of the compound system is described primarily by the compound nucleus cross section σ_c which is a function of incident energy only. In the simplest approximation the cross section is πR^2 where R is the radius of the target nucleus. Using $R=r_o A^{1/3}$ ($r_o=1.25\times10^{-13}$ cm. and A is the mass number of the target nucleus) yields a value of about 1.44 barns for σ_c which is in agreement with ENDF/B-V[35] evaluation for non-elastic neutron scattering. This simple model should be modified by the probability that the neutron enters a nucleus which it strikes, but this transmission coefficient (T_{in}) is nearly unity. Therefore

$$\sigma_c = \pi R^2 T_{in}$$

Although this quantity could in principle depend on incident energy, it is nearly constant throughout our energy range because we are well above the region where individual resonances cause fluctuations.

5.2 Decay of the Compound System

Once the compound system has formed, it will decay because it is unbound at these energies. An expression for the rate of decay has been developed by Weisskopf[36].

Consider the probability of the reverse process of the decay of the compound system, namely the capture of a neutron by the excited residual nucleus to form the compound system. The mean probability per unit time of capture of a neutron moving with velocity v by a nucleus enclosed in a volume V in the neutron energy interval dε about ε is

$$5.1 \qquad R_c(\varepsilon) = \sigma_c(E_c, \varepsilon) \frac{v}{V} .$$

The capture rate is the probability per unit time of the capture of a neutron by the excited residual nucleus. The capture rate can be related to the rate of the decay of the compound system using the principle of detailed balance[34].

$$5.2 \qquad \frac{R_c}{\rho_c} = \frac{R_d}{\rho_d}$$

where R_d is the probability per unit time for the decay of the compound system into a neutron and the excited residual nucleus. The density of states of the compound system is ρ_c and ρ_d is the density of states available to the decay.

This yields

$$5.3 \qquad R_d = R_c \frac{\rho_d}{\rho_c} \quad .$$

The density of states available to the decay of the compound system include those states in the residual nucleus (ρ_r) and those available in the volume V to the emitted neutron

$$5.4 \qquad \rho_n = \frac{V\, g\, m_n}{2\, \pi^2\, h^3} (2\, m_n\, \varepsilon)^{1/2}\, d\varepsilon$$

in the emitted neutron energy range ε to $\varepsilon + d\varepsilon$. Here V is a spherical volume enclosing the system, g is the number of neutrons per state (=2), and m_n is the mass of a neutron. Substituting equation 5.1 into 5.3 and separating the compound decay level density into those components due to the residual system and those due to the states available to the emitted neutron we obtain

$$5.5 \qquad R_d d\varepsilon = \sigma_c(E_c,\varepsilon) \frac{\rho_r}{\rho_c} \frac{V\, g\, m_n}{2\, \pi^2\, h^3} (2\, m_n\, \varepsilon)1/2 \frac{v}{V}\, d\varepsilon \quad .$$

Noting that $v = (2\varepsilon/m_n)^{1/2}$

5.6
$$R_d = \sigma_c(E_c,\varepsilon)\,\frac{\rho_r}{\rho_c}\,\frac{g\,m_n}{\pi^2 h^3}\,\varepsilon$$

To put the decay rate into a more standard and useful form the quantities $S_c(E_c)$ and $S_r(E_r)$ are defined as

5.7
$$S_c(E_c) = \ln \rho_c(E_c)$$
$$S_r(E_r) = \ln \rho_r(E_r)$$

such that S is analogous to the entropy. Using this 5.6 may be rewritten as

5.8
$$R_d = \sigma(E_c,\varepsilon)\,\frac{g\,m_n\,\varepsilon}{\pi^2\,h^3}\,e^{S_r(E_r)}\,e^{-S_c(E_c)}$$

Note that $E_r = E_c - \Delta E - \varepsilon$ (see figure 5.1) and therefore $S_r(E_r)$ can be expanded in a Taylor series about $E_c - \Delta E$ as

5.9
$$S_r(E_r) = S_r(E_c-\Delta E) - \varepsilon\,[dS_r / dE]_{E_c-\Delta E} + \Delta S$$

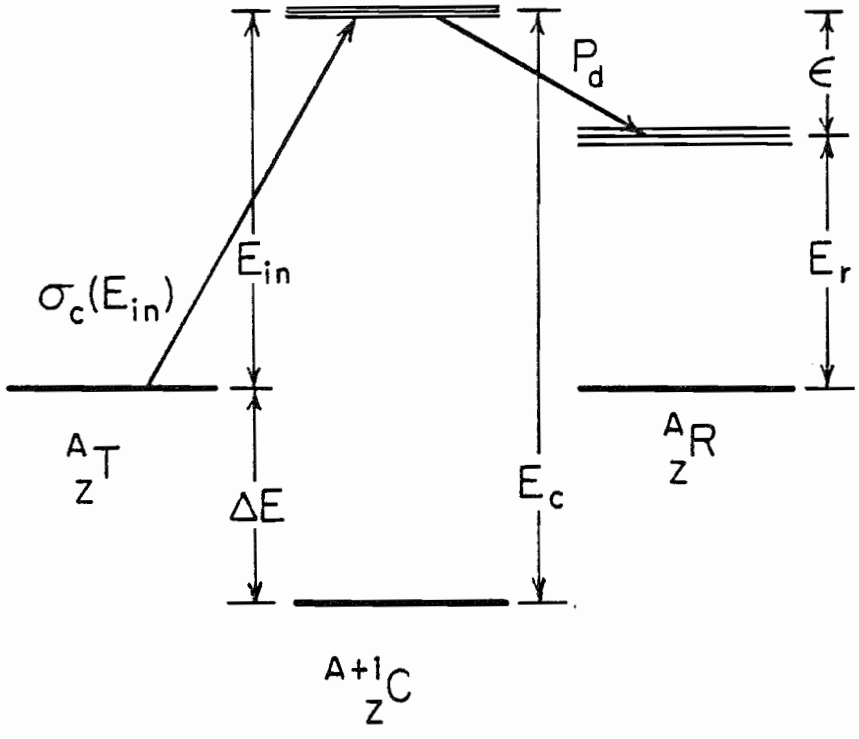

Figure 5.1 Schematic diagram for the compound inelastic scattering process. The target nucleus ($^{A}_{Z}T$) captures a neutron to form the excited compound system ($^{A+1}_{Z}C$) which subsequently decays to an excited state in the residual nucleus ($^{A}_{Z}R$).

where ΔS includes all further terms in the expansion. In analogy to thermodynamics, a temperature T can be defined

$$5.10 \qquad \frac{1}{T} = \frac{dS_r(E_c-\Delta E)}{dE}$$

such that T is the temperature of the residual nucleus with all of the energy of the neutron included (temperature at $E_r + \varepsilon$). Then by substituting equation 5.9 into 5.8.

$$5.11 \qquad R_d = \sigma(E_c,\varepsilon)\ \frac{g m_n e}{\pi^2 h^3}\ e^{S_r(E_c-\Delta E)-S_c(E_c)}\ \varepsilon\ e^{-\varepsilon/T(E_c-\Delta E)}\ e^{\Delta S}\ d\varepsilon$$

If the constant terms (those which do not depend on ε) are absorbed into a single constant (C) because the normalization will not be important we obtain

$$5.12 \qquad R_d = C\ \sigma(E_c,\varepsilon)\ \varepsilon\ e^{-\varepsilon/T}\ e^{\Delta S(\varepsilon,E_c;E_r)}$$

The simplest assumptions are made to simplify this expression. It is assumed that $\sigma(E_c,\varepsilon)$ does not depend on ε. It has already been assumed that the capture cross section of the target nucleus in the ground state does not depend on E_n which is the equivalent of ε for this process

($^{A}_{Z}T$ is the same nucleus as $^{A}_{Z}R$) and it therefore seems reasonable to make this assumption. Further, it is assumed that ΔS is small. In other words, that the Taylor series expansion is sufficiently accurate with only the first 2 terms. This assumption will depend on $E_c \gg \varepsilon$, which is true for low values of ε (the maximum value ε can have is about 1/2 the value of E_c for these experiments). The nuclear temperature T will also be assumed to be constant with outgoing neutron energy in analogy to the thermodynamics case. The expression 5.12 for the rate of decay becomes

$$R_d = C' \varepsilon e^{-\varepsilon/T} \quad . \tag{5.13}$$

The assertion is made that the only important channels for the decay of the compound system are those which emit neutrons. Charged particles have lower emission rates because they must penetrate the coulomb barrier to escape. Photons are observed to have lower emission rates so that neutrons are indeed the main channels for decay of the compound system. The probability of decay rate $R_d(\varepsilon)$ is integrated over all future time and normalized to a probability of decay $P_d(\varepsilon)$ which integrates to unity over all possible ε since the compound system must eventually

decay, it is unbound, and it will most likey emit a neutron. This yields

$$5.14 \qquad Pd(\varepsilon) = \frac{Rd(\varepsilon)}{\int_{\varepsilon=0}^{E_c-\Delta E} R_d(\varepsilon)\, d\varepsilon}$$

which is the probability of decay to be used.

5.3 Presentation of the Data

The results of the analysis of this data is the double differential scattering cross section. These results are shown in Figures 5.2-5.4 for iron and in Figures 5.5-5.7 for nickel. These data are the result of the analysis and corrections as described in Chapters IV and V. Each figure shows the result for one element and incident energy and each angle for which data analysis could be completed.

All data is presented in the laboratory reference frame and geometric corrections to the neutron exit angle have not been shown. Laboratory to center-of-mass frame conversions have not been made because this requires the assumption of the emission of only one neutron for each interaction. These transformation effects are generally small although the laboratory to center-of-mass frame energy shifts for

Figure 5.2 Double differential scattering cross sections for scattering of 7.5-MeV neutrons from iron at detector angles indicated. Note that each successive set has been plotted on a scale which differs by a factor of 10 from the one below it.

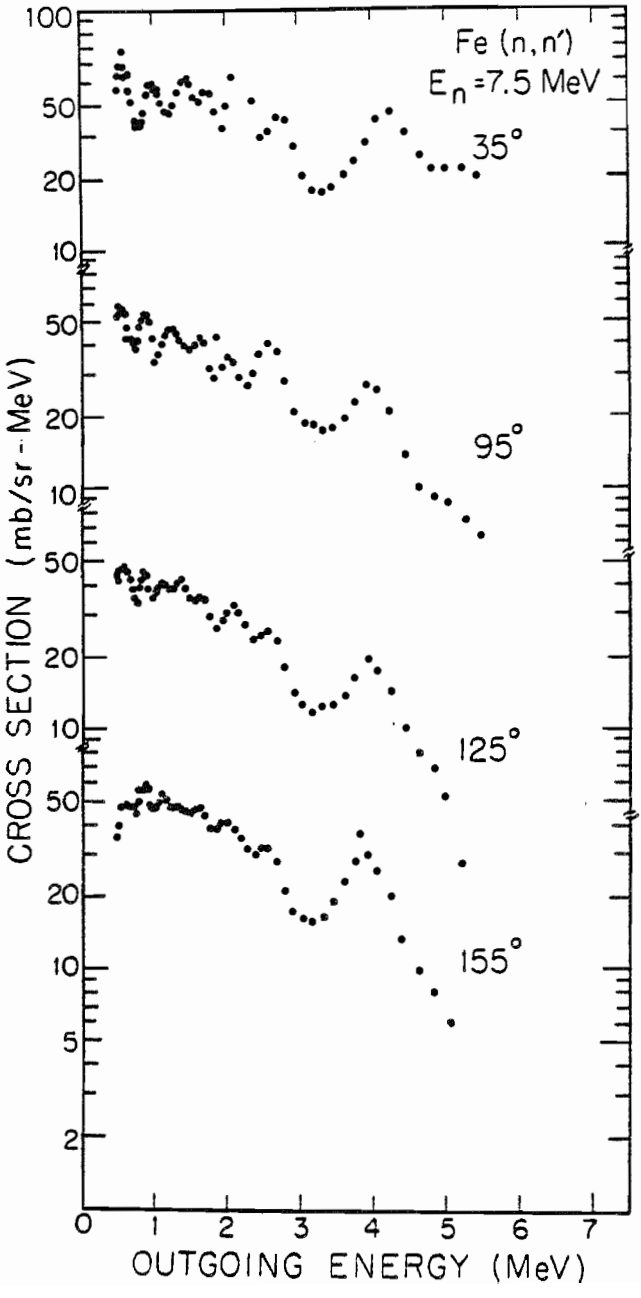
Fe (n,n')
E_n=7.5 MeV
35°
95°
125°
155°
CROSS SECTION (mb/sr-MeV)
OUTGOING ENERGY (MeV)
100
50
20
10
50
20
10
50
20
10
50
20
10
5
2
0
1
2
3
4
5
6
7

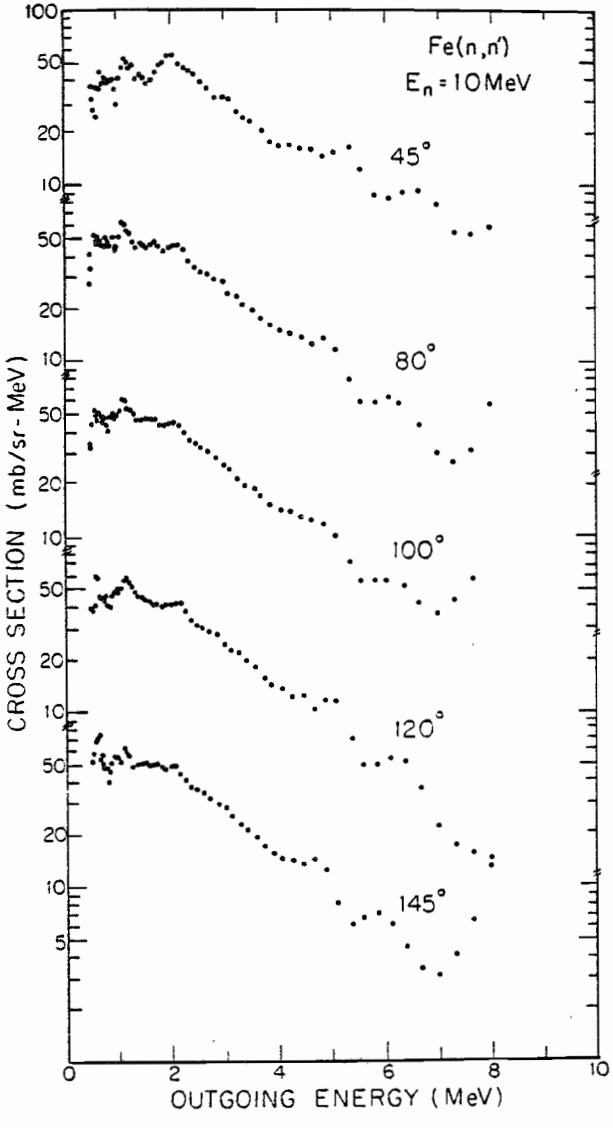

Figure 5.3 **Double differential neutron scattering cross sections for 10-MeV neutrons incident on iron for the scattering angles indicated.**

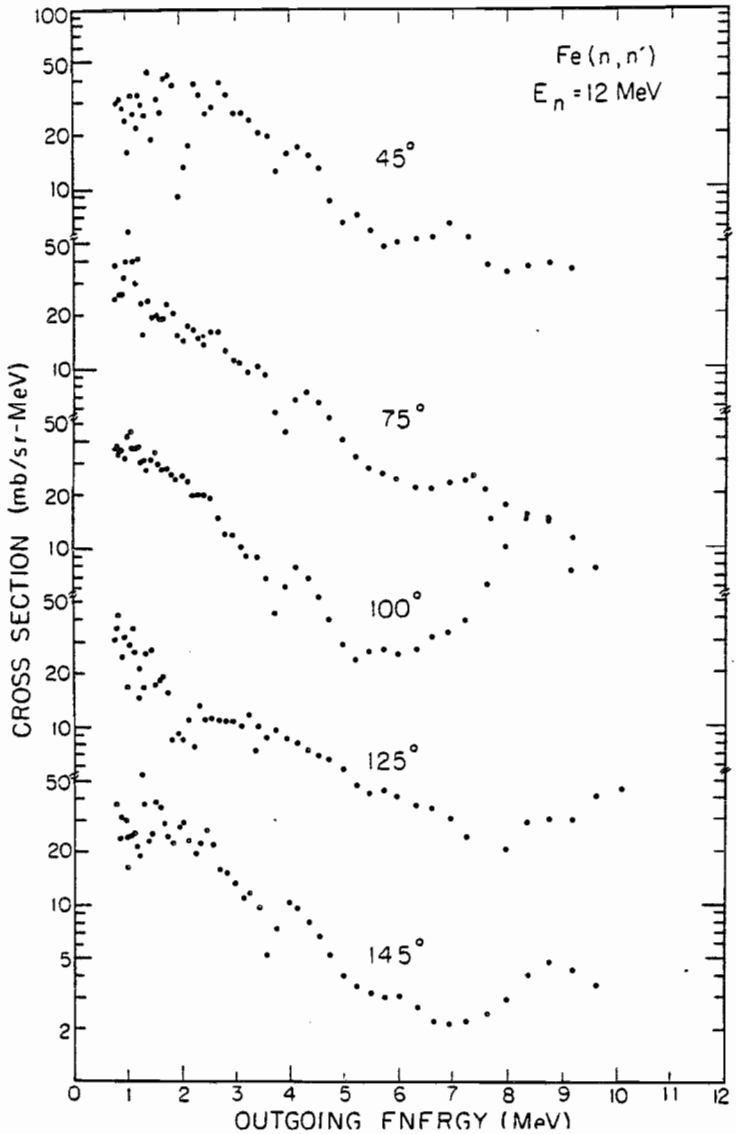

Figure 5.4 Double differential neutron scattering cross sections for 12-MeV neutrons incident on iron for the scattering angles indicated.

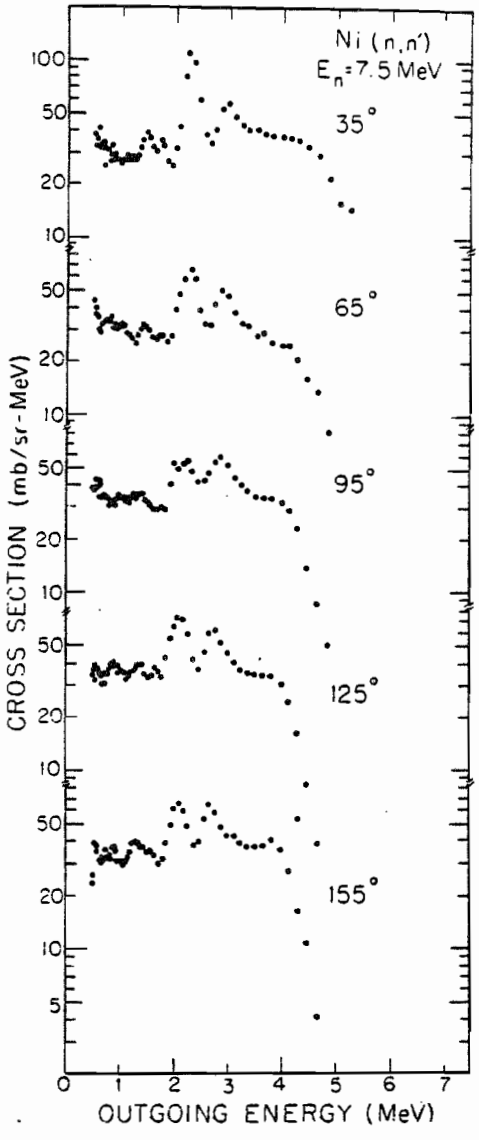

Figure 5.5 Double differential scattering cross sections for 7.5-MeV neutrons incident on natural nickel for the scattering angles indicated.

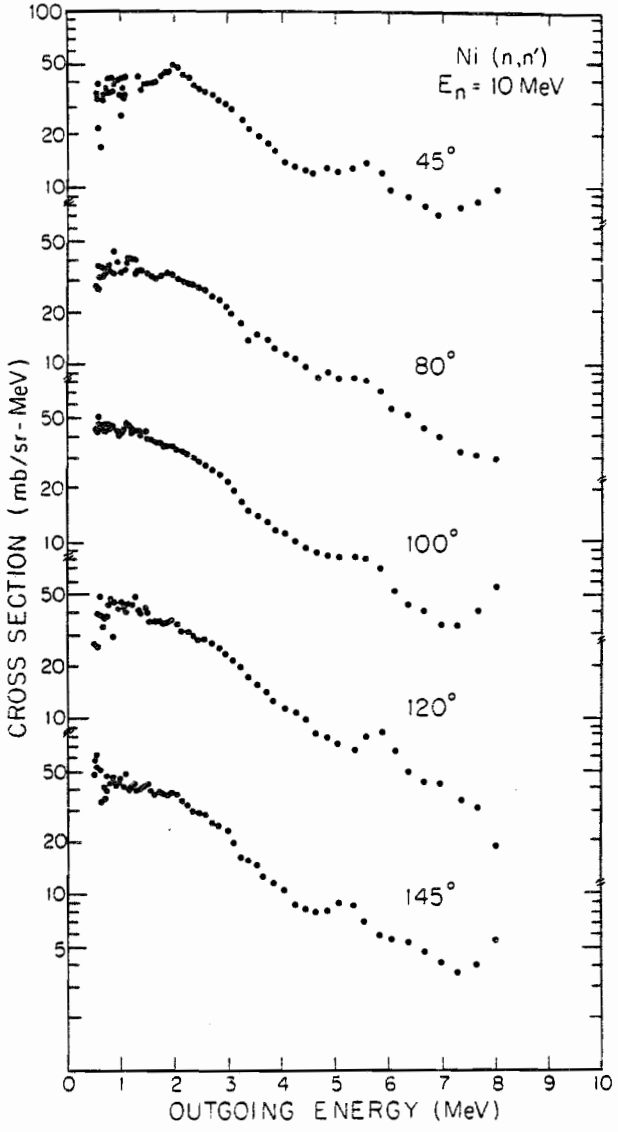

Figure 5.6 **Double differential scattering cross sections for 10-MeV neutrons incident on natural nickel for the scattering angles indicated.**

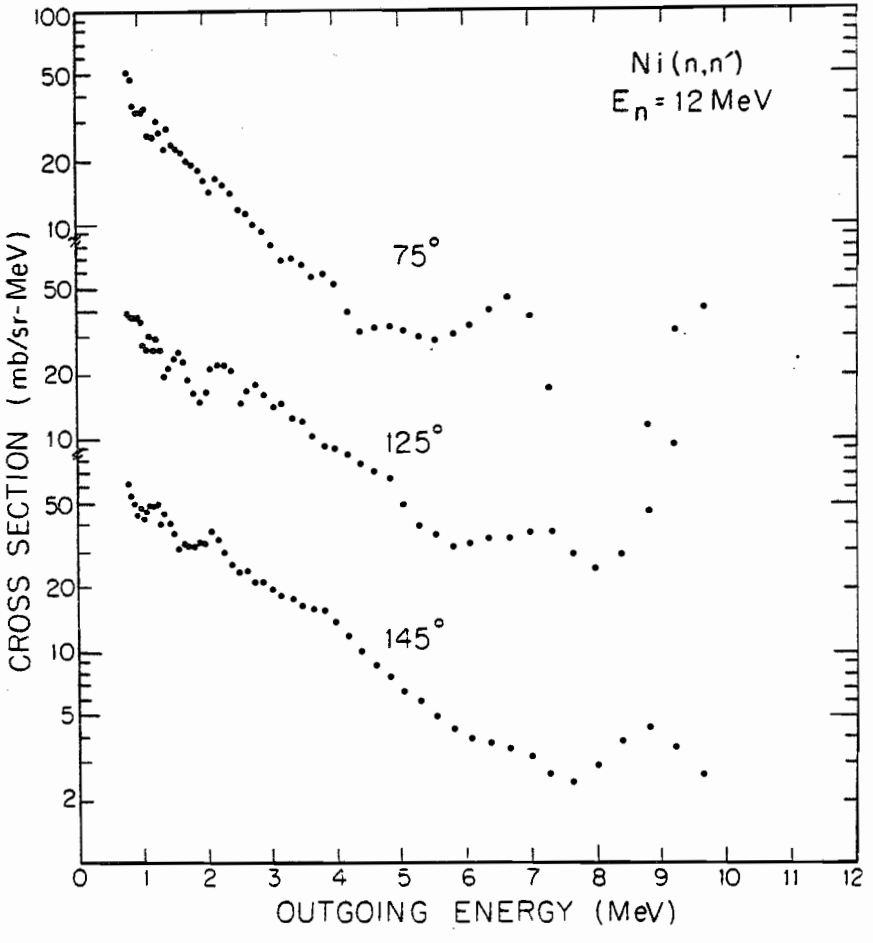

Figure 5.7 Double differential scattering cross sections for 12-MeV neutrons incident on natural nickel for the scattering angles indicated.

elastic and low-lying inelastic scattering reactions are several hundred kilovolts at large scattering angles. Geometric conversions, arrived at through the simulation, are usually small and the angle corrections (which are always less than 0.3^{o}) are dependent on the exit neutron energy.

Several important features of this data warrant brief discussion. In some cases, particularly at 12 MeV, very sharp low energy structure is shown. This is due, in large part, to subtraction problems (previously discussed in section 3.3). The subtraction problem results in structure that the computer program EFFIGYC tries to fit with cross section data that will agree with the observed structure after it has been smeared by the experimental conditions. This results in the data correction procedure reinforcing this structure which is merely an artifact of data reduction difficulties. Thus, if one averages this structure, it will result in the correct average cross section. Conversely, at the high energy end of the distributions, broad peaks appear. These are the result of sharp peaks in the time-of-flight spectra and the energy width shown corresponds to the time-resolution of the 256 channel spectra used in the correction. For exit energies higher than about 3-MeV residual nucleus excitation energy, the corrected cross sections become unreliable, particularly for the 12-MeV

data, due to difficulty in extracting the elastic and first-inelastic strength from the underlying strength. Since these discrete scattering cross sections are observed in these experiments to have strengths at least an order of magnitude higher than the observed continuum cross section, a small error in the magnitude of these discrete cross sections or in the peak shape can result in a large error in the extraction of the continuum strength from under discrete groups.

In addition to the energy distributions in Figures 5.2-5.7, the 10- and 12-MeV data is displayed in angular distribution form by averaging over one MeV intervals in the energy distributions. These angular distributions for the 10- and 12-MeV data are shown in Figures 5.8-5.11. These averages are performed by summing each energy bin (as displayed in figures 5.3, 5.4, 5.6, or 5.7), weighting by its width, and dividing by the number of bins summed. The 7.5 MeV data has not been displayed in this manner because the combination of structure and kinematic energy shifts make such figures misleading, no significant forward peaking is observed, and the structure causes the distributions to overlap leading to very confusing plots. As expected, the lowest exit neutron energies show essentially flat distributions or distributions which are flat about 90^{o}. At higher neutron exit energies, there is a significant trend

Figure 5.8 Double differential scattering cross sections averaged over 1 MeV intervals in exit neutron energy and plotted versus the cosine of laboratory scattering angle.

The meaning of the symbols are:

1 - Average cross section between 1 and 2 MeV.

2 - Average cross section between 2 and 3 MeV.

3 - Average cross section between 3 and 4 MeV.

4 - Average cross section between 4 and 5 MeV.

5 - Average cross section between 5 and 6 MeV.

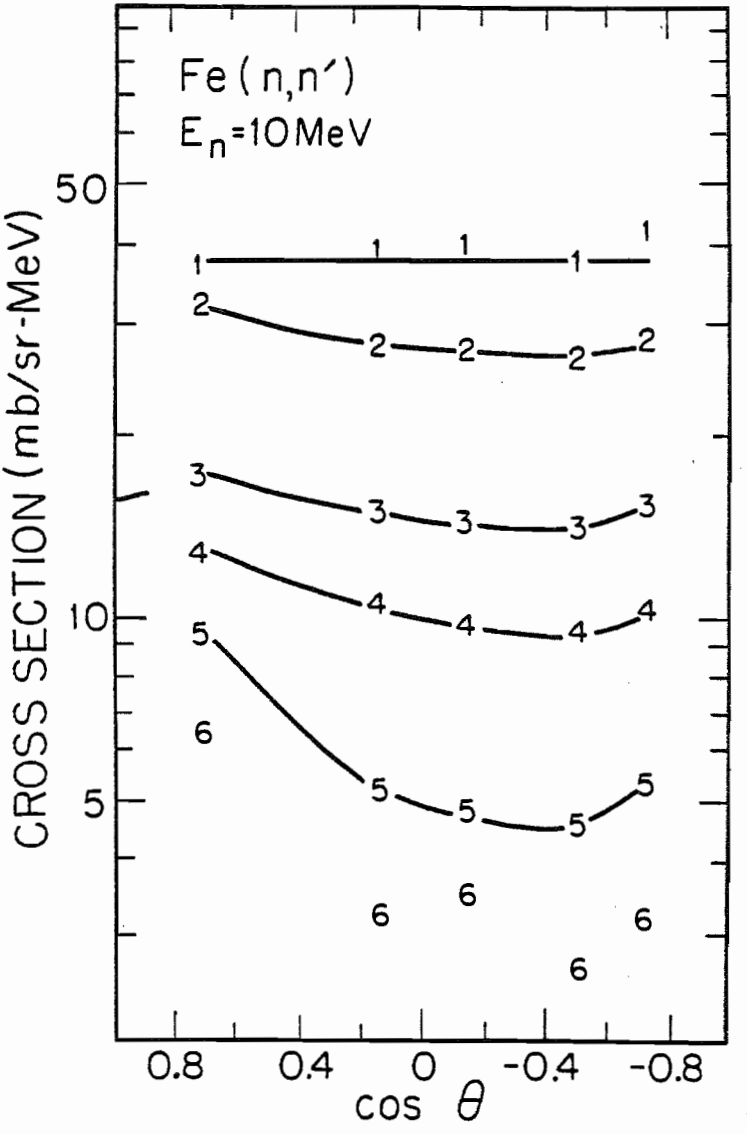
Fe (n,n′)
E_n=10MeV
CROSS SECTION (mb/sr-MeV)
50
10
5
0.8
0.4
0
-0.4
-0.8
cos θ
1
2
3
4
5
6

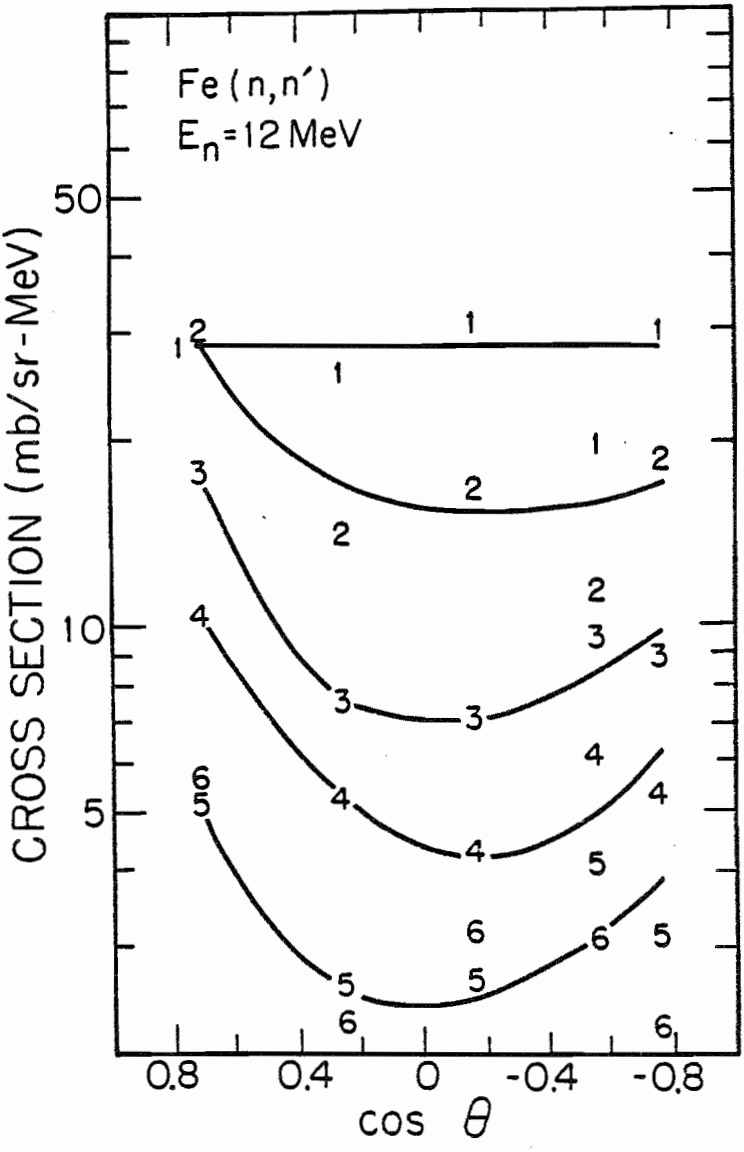

Figure 5.9 Double differential neutron scattering cross sections as in Figure 5.8 except for 12 MeV incident neutron energy.

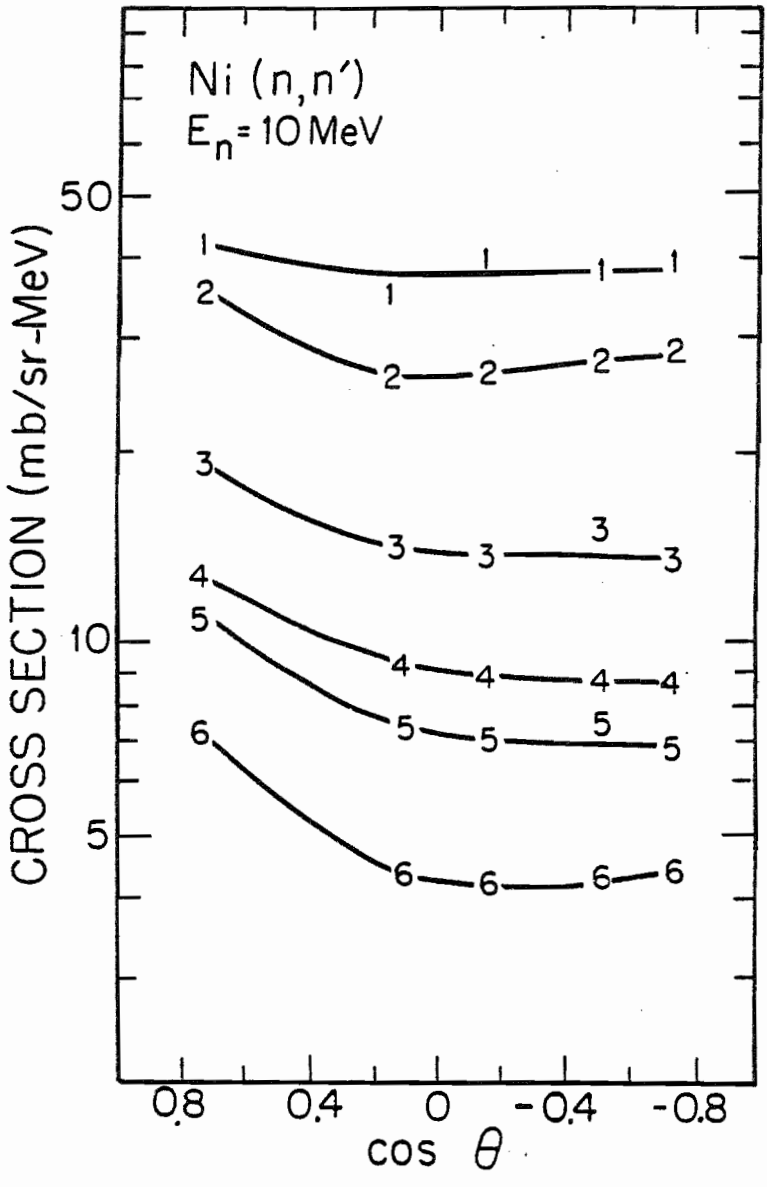

Figure 5.10 Double differential neutron scattering cross sections as in Figure 5.8 except for nickel.

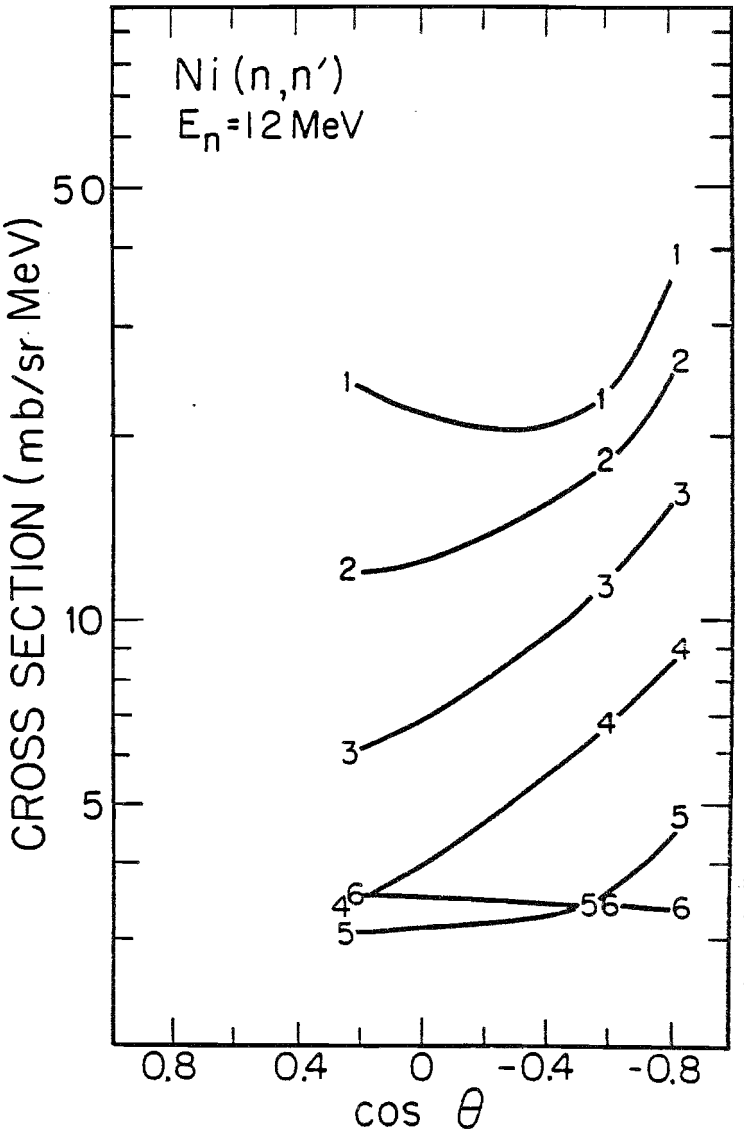

Figure 5.11 Double differential neutron scattering cross sections as in Figure 5.10 except for 12-MeV incident neutron energy.

toward forward peaking. This is particularly true of the 45^{o} points, but is also seen in the next forward-most angle. No complex angular distribution structure is expected and none is observed.

The data has been compared to several other similiar measurements and calculation. The results of these comparisons are shown in Figures 5.12 and 5.13. The data is presented as either angle integrated, angle averaged, or inferred angular integrated ($d\sigma/(dE\ d\Omega) \times 4\pi$) depending on the method by which the data were obtained. The data of this work is merely a typical angle near 90^{o} multiplied by 4π. The data of Owen and Towle[6] is their data for ^{56}Fe or ^{58}Ni at 95^{o} and 7.0 MeV multiplied by 4π. The ENDF-B/V[35] calculation is the ENDF-B/V angle integrated continuum neutron scattering distributions (MF = 3 and 4, MT = 91). which includes all single neutron evaporation events ((n,n')). The calculation of Vonach[37] are angle integrated values for use in corrections to his 14-MeV data. Vonach's calculation was interpolated between values at 14-, 11-, and 8-MeV to obtain values for comparison with this 10- and 12-MeV data but the comparison to this 7.5-MeV data is Vonach's 8-MeV calculation. The data of Kinney, et. al.[26] is angle averaged data times 4π where only points at every 100 KeV are shown. Due to this, Kinney's data appears to jump around, but the intermediate points seem to indicate

Figure 5.12 Comparison of these data with other data and calculations. The symbols have the following meanings.

• - Present work.

x - Vonach calculation[37].

⁀ - ENDF-B/V (file 3+4, section 91)[35].

Δ - Kinney and Perey[26].

\+ - Owen and Towle[6].

□ - Biryukov experimental data[13].

The 3 curves ([A], [B], and [C]) represent the 3 energies studied as indicated below with comments on the comparisons.

[A] includes these 12-MeV data at 125° and interpolation of the Vonach calculation between 11 and 14 MeV.

[B] includes these 10-MeV data at 100°, interpolation of Vonach calculation between 8 and 11 MeV, and Biryukov data at 9 MeV.

[C] includes these 7.5-MeV data at 95°, Vonach calculation at 8 MeV, ENDF-B/V interpolation between 7 and 8 MeV, and Owen and Towle data at 7.0 MeV.

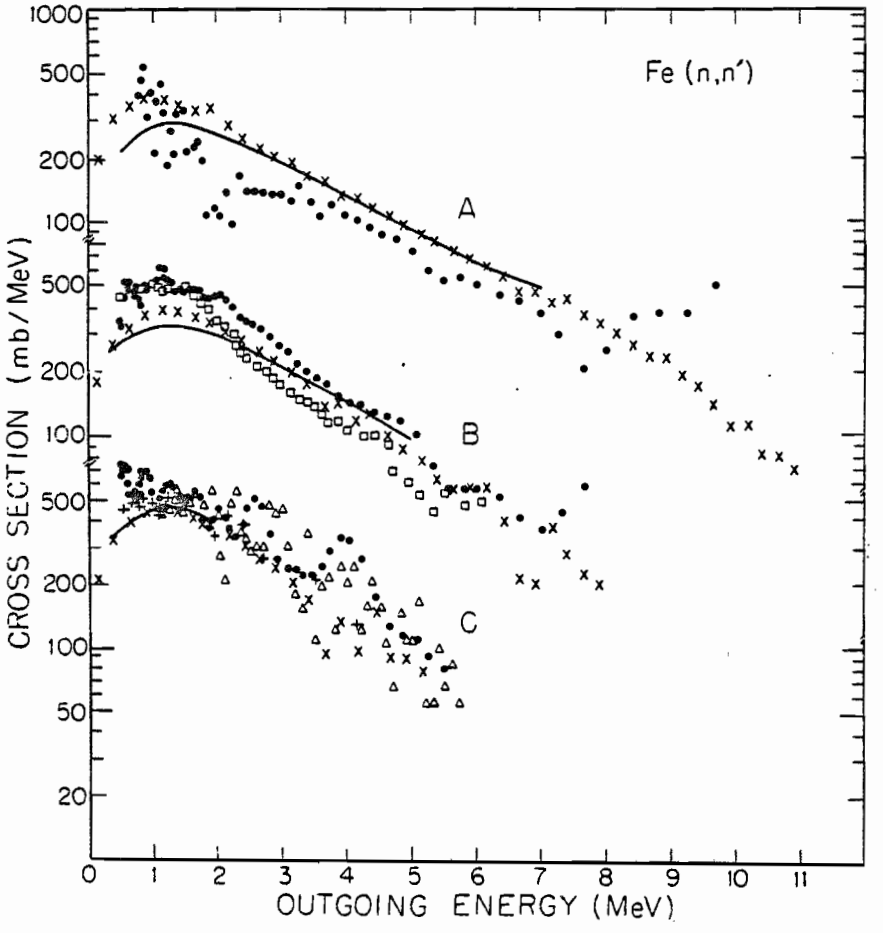
Fe (n,n')
A
B
C
CROSS SECTION (mb/MeV)
OUTGOING ENERGY (MeV)
1000
500
200
100
50
20
0
1
2
3
4
5
6
7
8
9
10
11

Figure 5.13 Comparison of the present work with other data and calculations. Symbols have the same meaning as Figure 5.12. Note that

[A] includes these data at 12 MeV and 75°.

[B] includes these data at 10 MeV and 100° and Biryukov data at 9 MeV.

[C] includes these data at 7.5 MeV and 95° and the data of Owen and Towle at 7.0 MeV for ^{58}Ni.

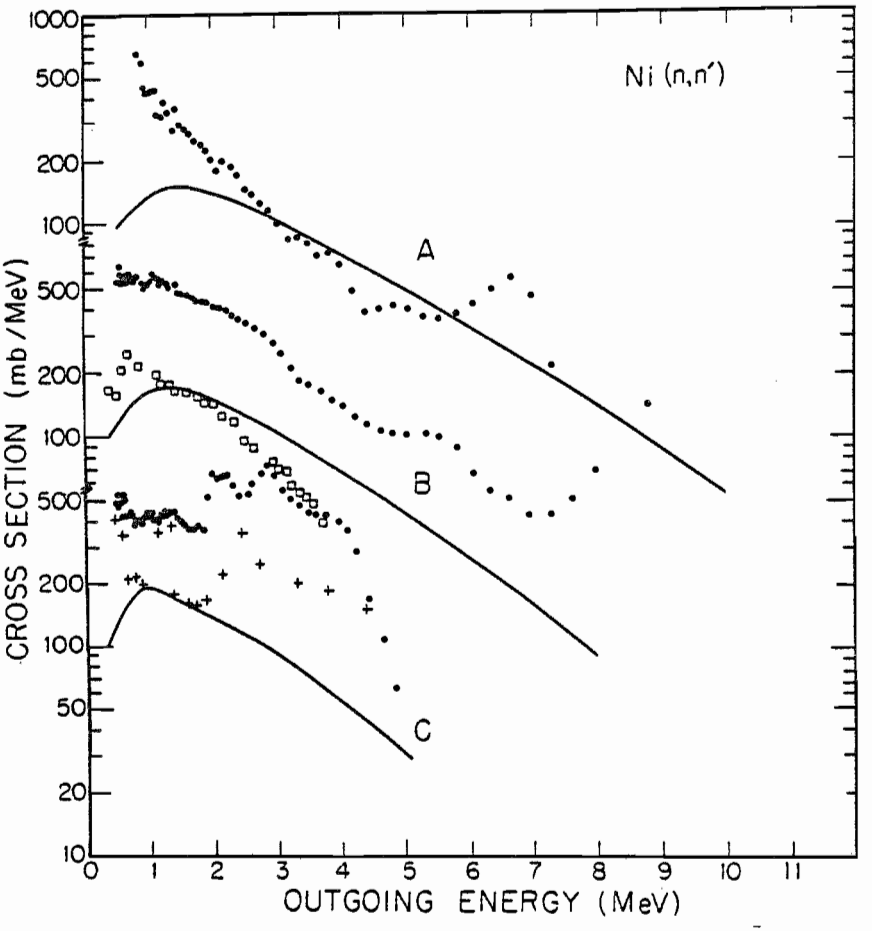
Ni (n,n')
A
B
C
CROSS SECTION (mb/MeV)
OUTGOING ENERGY (MeV)
1000
500
200
100
500
200
100
500
200
100
50
20
10
0
1
2
3
4
5
6
7
8
9
10
11

real structure seen with their superior resolution. Our data does not have good enough resolution to see most of this structure. The data of Biryukov[13] is 9-MeV experimental data, and is compared without alteration to our 10-MeV data. Agreement in the iron data is satisfactory. The nickel data shows a serious disagreement in magnitude but fair agreement in shape.

The spectral shapes are expected to fit the form of equation 5.13. In this form, if we divide the cross section by the outgoing energy and take the log of the result (or plot the result on a log scale) a straight line should result whose slope is the negative of the inverse of the nuclear temperature (-1/T). The results of such a linearization of the function and linear fit are shown in table 5.1 for various different regions in the data. In addition to the temperature, the normalization constant (C') (see equation 5.13) is also shown. The linear correlation coefficient (R_p) is the Pearson correlation coefficient produced by the computer subroutine LINFIT[38]. Values of R_p with absolute value near unity indicate a high correlation between the data and the straight line to which you are fitting. These temperatures, in the range 1.0 to 1.4, are consistent with the results of other measurements. Note however, that the temperature for the 7.5 MeV data, especially the nickel, is not in this range. It is not

Table 5.1 Nuclear temperature results from fits to the data over the ranges of exit neutron energies shown.

Element	Incident Energy (MeV)	Exit Energy Range (MeV)	Nuclear Temperature T (MeV)	Normal. Constant C'	Linear Correlation Coefficient R_p
Iron	7.5	1 -> 3	1.19 ±.47	93.1 ±68.	-.921
		1 -> 5	1.32 ±.19	78.4 ±28.	-.943
	10.0	1 -> 3	1.25 ±.15	82.2 ±25.	-.990
		1 -> 5	1.25 ±.15	82.2 ±25.	-.990
		1 -> 7	1.45 ±.09	56.3 ±12.	-.959
	12.0	1 -> 3	1.07 ±.29	63.2 ±33.	-.810
		1 -> 5	1.25 ±.11	45.5 ±12.	-.927
		1 -> 7	1.66 ±.11	24.3 ±4.3	-.899
		1 -> 9	2.11 ±.15	14.8 ±2.6	-.836
Nickel	7.5	1 -> 3	4.21 ±5.0	33.3 ±18.	-.510
		1 -> 4	2.52 ±1.0	43.5 ±17.	-.835
	10.0	1 -> 3	1.27 ±.46	84.4 ±48.	-.968
		1 -> 5	1.21 ±.13	88.5 ±27.	-.991
		1 -> 7	1.65 ±.10	46.0 ±9.7	-.960
	12.0	1 -> 3	.958 ±.34	77.0 ±58.	-.955
		1 -> 5	1.08 ±.12	59.0 ±22.	-.956
		1 -> 7	1.48 ±.14	26.7 ±7.8	-.922

expected that the results for spectra with such structure would be particularly meaningful. Some of the nuclear temperature fits are displayed in Figures 5.14 and 5.15 along with our data in the manner described above which should result in a straight line.

5.4 Discussion of the Uncertainties

The errors on this data are more difficult to evaluate than simply the statistics on the counting rates. In fact, random errors in counting statistics are a relatively small part of the total errors in some cases. These errors range from about 2% at the low energy end of the spectra, where count rates are highest, to 8% in the higest energy regions. Counting times were chosen on the basis of these statistical errors, therefore these errors do not vary appreciably between the various spectra. Another important source of error, is the error in the efficiency of the detectors. The largest efficiency errors are those for neutron energies below 1 MeV caused by difficulties in the efficiency measurements and the large changes in efficiency that can be caused by small bias changes. These errors, which are not statistical in nature but may change from run to run, are about 100% at 500 KeV and about 20% near the peak of the efficiency near 1 MeV. Errors at higher energies, are about

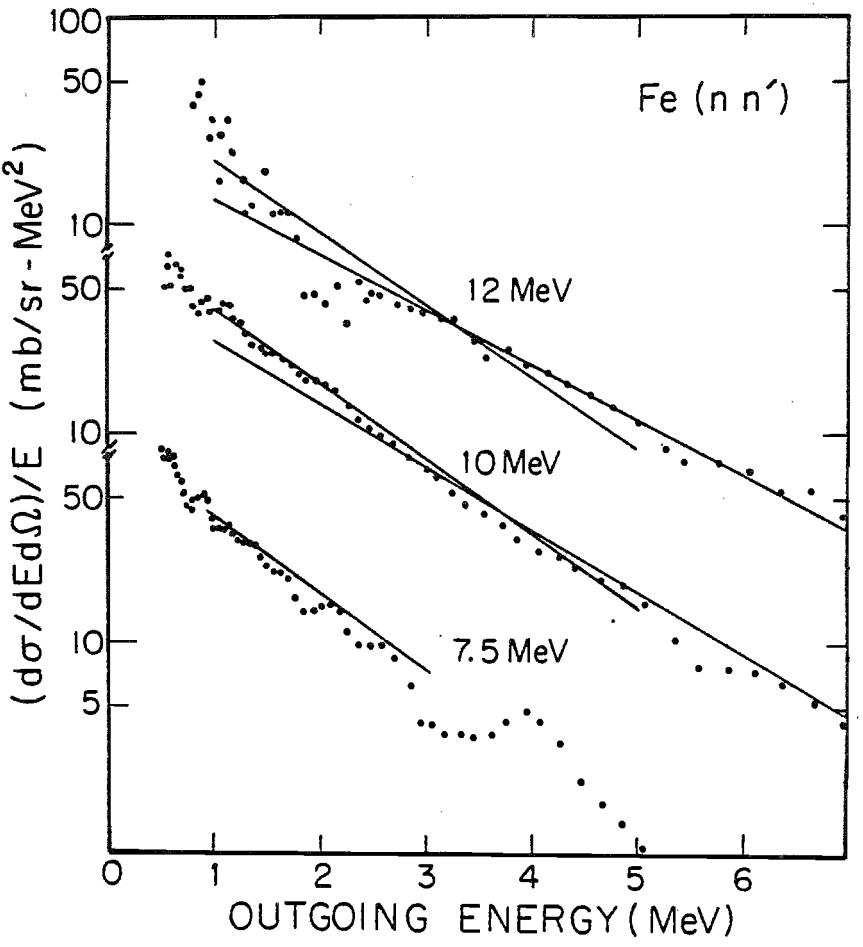

Figure 5.14 Nuclear temperature comparison for iron at the 3 incident energies studied. Lines indicate the fits to the data in the region over which the lines extend.

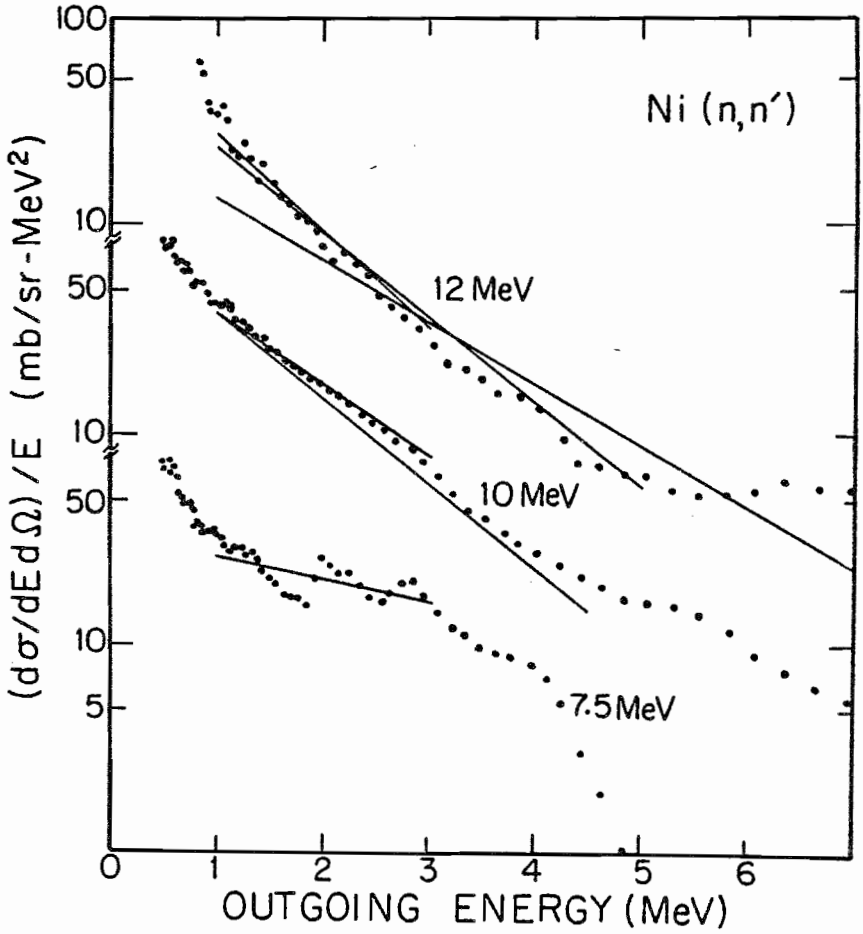

Figure 5.15 Nuclear temperature comparison for nickel at the 3 incident energies studied. Lines indicate the fits to the data in the region over which the lines extend.

3%. More information on detector efficiency will be presented by El-Kadi[5]. Another error is attributed to timing shifts, as has been previously discussed, which cause non-physical structure in the data which is further amplified in the correction procedure. These errors are not included in the errors listed in Appendix B. The corrections made to the data introduce other large sources of error to the data. The largest effect is that of attenuation of the incident flux. This is about a 30% correction throughout the continuum region and we believe we can make these corrections to within about a 5% error on the data (limited mainly by errors in the cross sections we need to make the corrections). There are other factors which call for less of a correction, yet introduce significant errors in the data. The effects of source gas-breakup neutrons contribute only in the lowest energy portions of the 10-MeV spectra and below about 2 MeV in the 12-MeV spectra. At their worst, their effect is less than 50%. However, we estimate that we can only make these corrections reliably to about 40% of their effect on the data. This implies a worst case error of about 20% on the data due to the source gas breakups, evident in the 12-MeV data below 2 MeV. Multiple scattering errors also present a problem, although they are more significant at the high energy end of the continuum where multiple scattering of the discrete groups is most important relative to the small value of the

cross section. These errors are estimated at about 5% at best, in the lower regions of the continuum, and 15% at worst in the highest regions of the continuum. These errors have been added in quadrature to arrive at the result shown in Appendix B. Another source of error is the normalization of the data to polyethylene. A correction to the normalization count rate of about 20% is probably the largest source of normalization error. The error in beam current integration is about 3%. This source of error is evaluated against monitor detector counts to arrive at this figure. The normalization experiment has the same set of difficulties encountered as the other scattering measurements with errors in efficiency and geometry corrections. The resultant error is believed to be about 15% in the normalization. Normalization errors are not present in the errors listed in Appendix B.

5.5 Conclusion

A comparison of these results with the work of others shows a fairly good agreement of the spectral shapes with that of the predictions. The nuclear temperatures (whose values are in the range of 1.0 to 1.4 MeV) are in agreement with other work primarily below 7.5 MeV and just above 14 MeV. The value obtained for the temperature depends on the

region over which the fit is made, with lower values of temperature for the lower energy ranges. Agreement in magnitude of the cross section for iron measured in this work with the work of others is within the errors of these experiments. Iron energy integrated yields exceed the upper limit of ENDF-B/V[35] total cross sections minus discrete state cross sections by less than 20%. The data for nickel, on the other hand, shows marked disagreement with the predictions particularly at 10 MeV, yet still is within about 10% of the of the total minus discrete state cross sections. (Nickel has other large contributors, particularly (n,p), so that the discrete state cross sections plus the continuum cross sections are not the only major contributors to the total cross sections.) It should be pointed out, in defense of the nickel data, that the raw data and corrections were very close to those of iron as is our final result.

The double differential cross sections for neutron scattering to the continuum has been a difficult experimental undertaking. The necessity of making these measurements in a configuration which has large undesirable contributions to the result is a major source of this difficulty. The development of experimental and computational systems to deal with these problems has been a major effort in this work. It is hoped that future

measurements of this type of cross section will be aided by this work.

Appendix A Multiple Scattering Rate Derivation

Consider scattering from a unit volume in the scatterer dV. Let

$$\frac{d^i R_i}{dV_{i-1}\, dV_i}$$

be the rate of scattering of the i^{th} order scattering per unit volume of the source sites dV_{i-1}, per unit volume of scattering sites dV_i. V_1 is the volume of the sample. V_2, ..., V_i are spherical volumes of fixed radius centered on the $(i-1)^{th}$ point. V_1 is treated differently than the other volumes because first scatterings are forced. The rate of scattering will be $R = \sum R_i$. The total rates R are expressed in equation A.1.

$$A.1 \quad R_i = \int_{V_1} \cdots \int_{V_i} dV_1 \cdots dV_i \; \frac{d^i R_i}{dV_1 \cdots dV_i}$$

This quantity can be expressed in terms of an average over volume in the form of equation A.2.

$$A.2 \quad R = \left\langle \frac{d^i R_i}{dV_1 \cdots dV_i} \right\rangle \quad V_1 \cdots V_i$$

Since the volumes in equation A.2 are constants they can be expressed explicitly.

$$A.3 \quad R = \left\langle \frac{d^i R_i}{dV_1 \cdots dV_i} \right\rangle \quad V_{samp}\, (4/3\ \pi R^3)^{i-i}$$

Consider the rate of scattering of i^{th} order scattering as in equation A.1. The first orders are expressed below in equations A.4.

A.4
$$\frac{dR_1}{dV_1} = F_{s1}\, T_{s1}\, \rho\, \frac{d\sigma_{1d}}{d\Omega}\, T_{1d}\, \Omega_{1d}\, \eta_{1d}$$

$$\frac{d^2R_2}{dV_1 dV_2} = F_{s1}\, T_{s1}\, \rho\, \frac{d\sigma_{12}}{d\Omega}\, \frac{T_{12}}{r_{12}^2}\, \rho\, \frac{d\sigma_{2d}}{d\Omega}\, T_{2d}\, \Omega_{2d}\, \eta_{2d}$$

$$\frac{d^3R_2}{dV_1 dV_2 dV_3} = F_{s1}\, T_{s1}\, \rho\, \frac{d\sigma_{12}}{d\Omega}\, \frac{T_{12}}{r_{12}^2}\, \rho\, \frac{d\sigma_{23}}{d\Omega}\, \frac{T_{23}}{r_{23}^2}\, \rho\, \frac{d\sigma_{3d}}{d\Omega}\, T_{3d}\, \Omega_{3d}\, \eta_{3d}$$

Note that the rates expressed in equation A.4 can be expressed in a general form as a function of i as in equation A.5.

A.5
$$\frac{d^iR_i}{dV_1 \ldots dV_i} = F_{s1}\, T_{s1}\, \rho\, \prod_{j}^{i-1}\, \rho\, \frac{d\sigma_{j,i+1}}{d\Omega}\, \frac{T_{j,i+1}}{r_{j,j+1}} \times \Omega_{id}\, \eta_{id}$$

We are interested in the average as in equation A.3, to enable evaluation of the integral in equation A.1. Substituting in for the rate obtained in equation A.5

equation A.6 is arrived at.

$$A.6 \quad R_i = \int_{r,\theta,\phi} F_{s1}\, T_{s1}\, \rho \prod_{k}^{i-1} \rho\, d\sigma_{k,k+1} \frac{T_{k,k+1}}{r^2_{k,k+1}}$$

$$\times\, \Omega_{id}\, \eta_{id} \prod_{k}^{i-1} r^2_{k,k+1}\, dr_k\, d\Omega_k$$

This result has the $1/r^2$ flux weight removed by the r^2 dependence of the volume element (by cancellation), eliminating the need to explicitly weight by the source point to sample point $1/r^2$ solid angle factor. This eliminates problems with computational overflow if the source point and sample point are chosen nearly the same. The other result of this cancellation is that the sample point selection must be chosen from uniform distribution in dr dΩ rather than a uniform distribution in volume. To enable Monte Carlo evaluation of this integral it must be transformed into the form of equation A.7 by the procedure

indicated in equation 4.3

A.7 R_i = [input to sample] x

$$x \left(\frac{4\pi R_c}{N}\right)^{i-1} \sum_{1}^{N} \prod_{k}^{i-1} \rho \frac{d\sigma_{k,k+1}}{d\Omega} T_{k,k+1}$$

x [exit from sample]

This expression is the sum that must be performed to evaluate the scattering weight. The input to sample and output from samples are not shown explicitly here but are shown in equation 4.4 They are indicated here to serve as a reminder that they must be included in the sum. Note that the i^{th} order scattering is related to the $(i-1)^{th}$ scattering rate involves only the i^{th} and $(i-1)^{th}$ scattering as indicated below.

A.8 $$\frac{R_1}{R_{i-1}} = 4\pi R_c \rho \frac{d\sigma_{i-1,i}}{d\Omega} T_{i-1,i}$$

With this result we can see that i^{th} order scattering can be calculated exclusive of the terms involving the final sample to detector interaction and the result saved. Then the final interaction can be put in for i^{th} order scattering and the factor in equation A.8 can be applied to the saved result to allow calculation of the $(i+1)^{th}$ order process. With this procedure the code can calculate to any order by

simply multplying by the appropriate factor. The code has a selection algorithm to allow choice of whether to calculate additional orders. The above discussion depends on forcing multiple scattering to occur inside a volume of fixed radius about the scattering sample and realizing that if a second scattering of interest does occur, it will occur inside of the sample, and thus our choice of the fixed radius appears in the result only as a scale factor. However it has been required that if a second event does occur, it must be one of the processes under consideration. We are not allowing for example (n,gamma), (n,p), or (n,n') processes not explicitly included. Therefore we must account for these losses to other channels at every interaction. This is done by scaling the result by the probability that an unaccounted for event occurs with the following factor.

A.9 $$\sum_i \frac{\sigma^i}{\sigma_{total}}$$

The sum over i of σ^i is the cross section for all processes under consideration at this incident energy and σ_{total} is the total cross section which is the cross section for any process to occur. The final ratio to apply to calculate i^{th} order scattering from $(i-1)^{th}$ order processes is shown

below.

$$\text{A.10} \qquad \frac{R_i}{R_{i-1}} = 4\pi R_c \rho d \frac{d\sigma_{i-1,i}}{d\Omega} T_{i-1,i} \frac{\sum \sigma^j}{\sigma_{total}}$$

With this result EFFIGY calculates first order scattering to the point of the first sample point using the method of equation A.5 then scales the result by the appropriate factors for a new choice for second scattering site as outlined in equation A.10

Appendix B Experimental Data

B.1 Iron at 7.5 MeV

Exit Energy	Angle 35.	95.	125.	155.	Percent Error
0.51	46.46	52.62	44.03	35.52	100
0.53	53.13	57.84	41.43	39.83	
0.55	56.56	54.79	45.37	46.57	
0.58	66.32	57.06	46.23	47.69	
0.60	57.38	54.53	47.20	48.09	
0.63	52.96	46.33	46.31	48.10	
0.65	52.88	41.96	44.50	46.76	
0.68	46.48	42.53	41.72	46.60	
0.71	41.48	40.65	37.93	46.95	
0.74	34.68	38.48	34.67	44.48	
0.77	33.16	41.06	34.10	47.94	
0.80	33.50	47.25	38.44	54.90	75
0.84	34.04	50.61	42.25	54.72	
0.87	37.47	53.76	44.94	57.31	
0.91	44.61	53.56	44.27	55.26	
0.95	48.88	49.65	37.94	48.09	
0.99	49.18	42.89	35.49	46.55	
1.03	46.36	33.59	37.17	46.37	50
1.08	45.00	35.89	38.57	49.30	
1.12	41.03	40.21	40.43	53.83	
1.17	37.53	44.21	39.75	50.87	
1.22	36.82	46.33	38.43	47.58	20
1.27	39.61	46.44	38.74	47.59	
1.33	45.22	44.61	40.71	46.96	
1.38	49.63	41.25	41.98	46.13	
1.44	51.18	39.44	38.50	44.97	
1.50	48.64	38.56	35.05	44.50	15
1.57	42.54	40.27	34.72	46.12	
1.64	41.60	42.79	35.60	46.73	
1.70	44.73	40.95	34.39	43.11	
1.78	46.00	31.56	29.27	38.05	
1.85	37.46	29.22	26.34	37.67	
1.93	31.32	32.02	27.89	40.01	
2.01	39.44	35.62	30.34	40.02	10
2.10	52.83	33.71	32.21	37.51	
2.19	63.63	28.79	30.84	34.79	
2.28	60.65	26.80	26.11	31.02	
2.38	41.37	30.26	23.75	29.65	
2.48	29.35	36.68	24.71	31.40	
2.59	30.84	40.35	25.50	31.46	
2.70	34.81	37.34	23.37	27.62	
2.81	33.94	27.84	17.92	20.96	
2.93	27.02	20.68	14.14	17.23	
3.06	20.23	18.96	12.75	16.22	

3.19	17.58	18.57	11.91	15.83	
3.32	17.40	17.86	12.55	16.19	
3.46	18.28	18.13	12.34	18.75	
3.61	20.25	19.88	13.54	22.62	
3.77	23.11	23.04	16.38	27.46	
3.93	27.52	26.79	19.28	29.57	
4.09	34.15	25.85	17.52	25.57	
4.27	36.11	20.98	14.33	19.90	10
4.45	29.80	14.03	10.03	13.16	
4.64	24.10	10.30	7.89	9.88	20
4.84	21.84	9.32	6.80	7.99	
5.04	21.78	8.89	5.23	6.00	50
5.26	21.77	7.34	2.71	3.06	
5.48	20.09	5.75	0.18	0.18	100

B.2 Iron at 10 MeV

Exit Energy	Angle 45.00	80.00	100.00	120.00	145.00	Percent Error
0.51	29.51	22.31	26.67	31.36	42.20	100
0.53	29.46	32.92	27.15	30.84	46.55	
0.56	25.15	27.26	35.24	34.76	54.92	
0.58	21.64	40.04	41.59	48.36	55.94	
0.61	19.81	45.62	39.47	46.99	59.56	
0.64	29.19	38.81	37.31	36.78	44.00	
0.67	28.68	43.80	40.28	36.14	45.75	75
0.70	35.40	37.37	38.83	36.31	40.56	
0.73	30.50	33.80	36.11	35.22	37.43	
0.76	32.41	35.91	37.64	37.52	37.31	
0.80	32.11	40.25	34.23	32.96	32.05	
0.84	31.03	38.21	31.98	32.27	37.13	
0.87	31.29	36.69	38.14	37.29	41.84	
0.91	32.23	40.78	40.09	39.25	45.62	
0.96	28.21	33.67	37.81	41.17	44.85	
1.00	23.21	38.05	39.20	38.74	44.69	50
1.05	32.99	41.01	41.35	41.07	42.39	
1.10	37.76	49.04	48.73	45.81	50.14	
1.15	41.89	48.48	47.96	47.02	46.44	
1.20	40.06	43.66	43.02	44.23	46.30	20
1.26	37.22	42.88	42.48	42.59	45.04	
1.31	38.43	38.29	40.14	39.51	38.37	
1.37	32.63	35.99	36.90	36.87	41.18	
1.44	34.38	37.60	37.27	36.55	40.87	
1.50	33.07	36.80	37.32	35.47	41.48	10
1.57	30.56	36.02	37.85	34.49	40.15	
1.65	31.79	37.87	37.41	33.36	40.47	
1.72	35.48	38.97	36.92	33.66	41.09	
1.80	39.14	36.43	34.91	32.54	38.99	
1.88	39.92	34.46	34.73	33.04	38.31	
1.97	43.18	35.51	35.55	33.20	40.15	
2.06	43.08	36.72	35.80	33.82	39.95	
2.16	39.46	36.90	34.69	33.55	35.92	
2.26	37.36	34.71	31.51	30.42	32.55	
2.36	36.15	29.60	28.26	27.02	30.22	
2.47	34.40	27.06	26.75	25.21	29.13	
2.59	31.43	25.89	25.75	24.33	27.96	
2.70	28.57	25.20	24.50	23.26	25.93	
2.83	25.35	23.83	22.54	22.38	23.89	
3.00	25.43	22.76	20.61	19.71	22.95	
3.10	24.91	19.49	19.45	18.41	20.59	
3.24	21.27	18.51	17.09	17.74	18.38	
3.39	19.71	16.58	15.46	16.04	17.20	
3.55	18.67	15.49	14.96	14.72	15.59	
3.71	15.97	14.37	13.61	12.65	13.90	
3.88	14.29	12.79	12.23	11.46	12.59	
4.06	13.57	11.82	11.33	10.90	11.73	
4.25	13.64	11.64	11.06	10.18	11.30	

4.44	13.30	11.01	10.31	9.77	10.97	
4.65	12.94	10.16	9.74	8.38	11.63	
4.87	11.91	10.66	9.50	9.33	10.08	
5.09	12.63	9.31	8.08	9.22	6.47	
5.33	13.51	6.29	5.61	5.71	4.92	
5.57	9.93	4.62	4.47	3.92	5.38	
5.83	7.11	4.66	4.53	4.00	5.69	
6.10	6.76	4.97	4.55	4.36	4.91	
6.38	7.27	4.60	4.16	4.16	3.62	10
6.68	7.42	3.41	3.32	2.93	2.72	
6.98	6.31	2.38	2.91	1.75	2.52	
7.31	4.65	2.08	3.49	1.37	3.27	
7.64	4.16	2.47	5.10	1.27	5.25	
8.00	4.63	4.59	8.19	1.05	11.80	50
8.37	4.00	8.53	9.77	1.82	11.68	
8.75	2.97	10.31	9.22	2.33	7.17	100

B.3 Iron at 12 MeV

Exit Energy	Angle 45.	75.	100.	125.	150.	Percent Error
0.83	30.07	37.95	36.02	35.84	19.01	80
0.87	31.15	25.70	33.14	42.38	23.45	
0.92	27.58	25.74	35.09	24.26	30.46	
0.96	23.74	32.40	31.67	31.30	29.86	
1.01	15.90	39.51	40.94	16.76	16.04	
1.06	32.95	58.50	42.16	28.74	24.16	
1.11	25.71	39.50	35.93	35.44	32.94	
1.16	21.67	29.78	36.11	26.14	21.37	
1.22	33.21	40.11	37.06	14.47	26.87	50
1.27	29.10	23.19	30.22	20.92	54.63	
1.34	25.42	15.34	30.76	16.58	36.57	
1.40	43.92	24.51	27.01	25.96	22.69	
1.47	18.43	19.69	31.23	26.90	24.80	
1.54	30.53	19.52	34.17	17.17	37.53	30
1.61	26.11	18.44	29.15	18.27	35.04	
1.69	40.21	18.41	27.37	18.92	28.52	
1.77	40.84	22.65	27.42	15.41	23.83	
1.86	37.31	20.58	25.34	8.57	21.84	
1.95	8.97	15.34	23.89	9.05	26.94	
2.04	13.08	14.60	25.07	8.54	28.05	20
2.14	17.04	17.48	23.40	10.91	22.71	
2.24	37.73	16.76	19.51	7.66	19.05	
2.35	33.06	14.78	19.83	12.89	21.84	
2.47	25.85	13.45	19.80	11.04	25.71	
2.58	27.84	15.82	18.56	11.88	21.24	10
2.71	38.57	16.09	14.50	11.46	15.35	
2.84	33.22	12.75	11.98	11.39	14.89	
2.98	26.03	11.10	11.80	11.48	13.20	
3.12	25.88	10.74	9.90	10.98	10.94	
3.27	23.49	9.64	8.75	11.74	11.41	
3.43	20.08	10.30	8.78	9.83	9.55	
3.59	19.43	9.18	6.72	8.63	5.15	
3.77	12.22	5.58	4.32	9.57	7.22	
3.95	15.38	4.39	6.11	8.65	10.26	
4.14	16.92	6.72	7.73	8.08	9.48	
4.34	15.25	7.39	6.74	7.41	7.79	
4.55	12.94	6.29	5.31	6.86	6.56	
4.77	8.50	5.31	3.93	6.54	5.15	
5.00	6.55	3.97	2.89	5.78	3.94	
5.24	7.06	3.15	2.37	4.62	3.46	
5.49	5.82	2.82	2.62	4.19	3.12	
5.76	4.76	2.55	2.67	4.31	2.95	15
6.03	5.01	2.32	2.52	3.99	3.05	
6.33	5.19	2.12	2.67	3.58	2.63	
6.63	5.27	2.10	3.11	3.50	2.15	
6.95	6.32	2.28	3.29	3.01	2.10	
7.29	5.33	2.32	3.85	2.31	2.18	30
7.64	3.65	2.07	6.05	1.64	2.41	

8.01	3.42	1.72	9.85	2.00	2.92	
8.39	3.62	1.51	14.47	2.88	3.99	
8.80	3.78	1.35	14.03	3.02	4.72	50
9.22	3.50	1.10	7.19	2.95	4.30	
9.67	6.87	0.75	1.53	4.04	3.48	
10.13	14.97	0.28	0.00	2.87	2.32	
10.62	17.98	0.02	0.00	0.96	1.51	100

B.4 Nickel at 7.5 MeV

Exit Energy	Angle 35.	65.	95.	125.	155.	Percent Error
0.51	38.29	43.86	37.65	34.52	23.30	100
0.54	32.69	39.89	37.31	36.42	25.76	
0.56	35.56	36.63	42.27	32.49	38.56	
0.58	41.28	35.93	38.38	38.64	37.99	
0.60	31.93	30.16	42.19	37.08	34.76	
0.63	33.57	29.28	39.77	34.97	31.02	
0.65	34.06	32.79	33.64	33.89	30.51	
0.68	25.49	33.37	33.80	30.33	32.46	75
0.71	31.87	33.69	34.07	30.65	31.74	
0.74	31.09	33.65	34.42	35.21	31.84	
0.77	26.91	33.05	34.06	34.51	36.21	
0.80	29.02	32.93	30.16	36.78	33.05	
0.83	32.90	35.59	32.15	40.14	31.52	
0.87	29.42	30.28	31.83	40.93	36.61	
0.90	27.38	31.72	30.75	38.47	36.89	
0.94	27.55	30.12	32.71	38.65	34.39	
0.98	25.93	31.19	34.80	34.98	30.42	
1.02	27.74	32.43	33.80	35.96	30.44	
1.06	28.78	31.73	33.99	35.48	29.25	50
1.10	27.46	28.69	32.52	32.44	30.91	
1.15	27.56	27.89	31.45	33.89	32.03	
1.19	28.64	26.87	34.05	35.57	35.06	
1.24	27.71	25.20	35.56	36.62	38.48	20
1.29	29.45	27.92	33.50	37.60	39.29	
1.34	32.28	29.95	34.98	39.42	39.39	
1.40	35.69	32.16	35.40	38.99	37.43	
1.46	39.11	31.43	32.37	34.97	36.32	
1.52	36.67	29.81	31.28	33.10	34.82	15
1.58	32.01	27.52	30.66	33.94	35.17	
1.64	30.50	26.87	28.95	37.81	33.31	
1.71	35.32	27.96	29.12	35.92	29.41	
1.78	33.14	27.64	30.06	33.22	31.28	
1.85	26.61	25.73	28.80	42.89	39.31	
1.93	25.46	28.25	40.75	55.09	49.47	
2.01	32.53	38.94	52.92	63.93	61.59	10
2.09	42.77	47.74	50.45	71.83	64.55	
2.17	79.75	58.71	51.89	71.11	59.46	
2.26	110.17	66.17	52.40	58.20	48.46	
2.35	95.58	58.35	46.29	41.49	37.90	
2.44	58.91	38.94	41.75	36.55	39.78	
2.55	37.67	32.28	42.29	46.12	53.78	
2.65	34.14	32.02	46.57	59.53	63.76	
2.76	40.27	40.80	53.87	61.54	57.85	
2.87	53.26	50.84	57.88	51.66	47.90	
2.99	56.46	47.32	51.19	45.34	43.33	
3.11	47.81	37.93	43.82	39.92	42.53	
3.24	40.90	33.21	40.16	37.05	38.74	
3.37	40.22	31.84	37.42	35.62	37.11	

3.51	40.18	28.34	34.96	34.72	37.54	
3.65	38.85	28.86	33.89	33.85	37.80	
3.80	37.42	25.84	33.80	33.84	40.06	
3.96	37.32	24.84	32.21	30.52	36.36	
4.12	36.99	25.21	28.75	24.37	27.46	20
4.28	35.82	20.77	22.97	16.38	16.42	
4.46	33.34	15.98	13.57	8.42	10.83	50
4.64	29.44	13.56	8.83	3.87	4.16	
4.83	22.26	8.22	4.81	0.00	0.00	100

B.5 Nickel at 10 MeV

Exit Energy	Angle 45.	80.	100.	120.	145.	Percent Error
0.51	31.86	29.05	42.98	25.96	47.42	100
0.53	38.21	37.33	41.78	25.25	56.69	
0.56	32.61	27.36	46.43	38.88	61.84	
0.58	21.67	31.86	48.84	48.16	52.00	
0.61	16.97	36.34	43.33	37.98	50.87	
0.64	34.44	35.17	43.24	32.95	33.84	
0.67	31.22	33.08	45.23	37.43	40.66	
0.70	36.25	32.80	42.72	34.36	34.84	
0.73	41.42	35.67	46.79	37.47	38.84	
0.76	35.10	36.96	45.71	43.25	46.23	
0.80	41.63	34.04	41.48	39.04	42.84	75
0.84	35.80	33.12	45.11	37.36	43.36	
0.87	39.31	41.88	46.70	45.75	46.20	
0.91	40.24	37.84	42.88	41.60	41.82	
0.96	33.88	34.81	39.93	41.09	42.93	
1.00	26.07	34.42	41.72	45.14	45.24	
1.05	34.16	34.37	43.25	42.48	40.37	
1.10	42.58	37.99	47.44	39.83	48.35	
1.15	42.88	40.49	44.80	43.74	38.20	
1.20	37.16	40.17	42.21	43.09	40.34	20
1.26	32.10	40.16	43.64	48.29	42.71	
1.31	44.43	34.29	42.07	40.04	38.95	
1.37	36.81	33.24	40.06	39.41	40.02	
1.44	39.46	34.92	41.48	41.75	41.44	
1.50	39.51	32.83	38.05	39.47	42.71	10
1.57	39.84	32.52	38.02	35.61	38.59	
1.65	40.57	31.53	36.87	35.52	36.83	
1.72	43.07	33.03	36.75	35.07	38.33	
1.80	45.29	33.00	35.20	34.62	37.24	
1.88	45.65	33.90	35.01	35.07	36.11	
1.97	49.64	32.83	35.03	36.46	37.42	
2.06	48.01	30.98	33.01	34.26	36.99	
2.16	44.21	30.01	32.65	31.74	34.05	
2.26	41.44	28.80	31.57	31.23	31.74	
2.36	37.54	28.28	29.74	29.67	29.65	
2.47	36.15	27.55	28.81	28.04	29.20	
2.59	35.32	26.47	27.38	28.17	28.33	
2.70	33.72	24.64	25.88	26.78	25.46	
2.83	31.39	23.58	24.46	25.05	24.22	
2.96	29.48	20.99	22.09	23.11	22.83	
3.10	28.12	19.87	19.75	21.42	19.28	
3.24	24.36	16.97	16.78	19.39	15.86	
3.39	21.49	14.11	15.01	17.07	15.43	
3.55	19.89	14.90	14.24	15.48	14.64	
3.71	17.87	13.68	12.87	14.30	12.52	
3.88	15.99	12.48	11.88	12.51	11.51	
4.06	14.18	11.59	11.21	11.31	10.47	
4.25	13.21	10.54	10.25	10.74	8.74	

4.44	12.78	9.63	9.49	9.79	8.22	
4.65	12.20	8.69	8.69	8.20	7.93	
4.87	12.86	8.86	8.16	7.59	7.99	
5.09	12.44	8.52	8.12	7.04	8.97	
5.33	12.97	8.12	8.08	6.74	8.60	
5.57	14.05	8.18	7.75	7.85	6.87	
5.83	11.96	6.87	6.78	8.51	5.81	
6.10	9.69	5.61	5.42	6.56	5.55	
6.38	8.78	5.21	4.74	4.95	5.26	10
6.68	7.91	4.55	4.23	4.34	4.73	
6.98	7.15	3.94	3.76	4.15	4.03	
7.31	7.07	3.26	3.65	3.77	3.53	
7.64	8.25	3.06	4.16	3.13	3.90	
8.00	9.57	2.64	4.85	1.89	5.47	50
8.37	14.52	1.61	3.28	0.00	6.89	
8.75	17.77	1.08	2.64	0.00	7.03	100

B.6 Nickel at 12 MeV

Exit Energy	|<------ Angle ------>| 75.	125.	145.	Percent Error
0.84	51.14	38.05	61.01	80
0.88	47.12	37.20	53.95	
0.92	35.35	36.83	49.39	
0.96	33.55	36.80	44.06	
1.01	33.45	35.51	47.21	
1.05	38.53	27.27	42.54	
1.10	34.12	25.94	45.43	
1.15	26.11	29.92	48.81	
1.21	25.78	27.77	48.61	50
1.27	30.68	29.26	49.28	
1.33	26.81	25.86	39.37	
1.39	22.32	19.39	44.35	
1.45	27.77	21.23	40.58	
1.52	23.19	23.24	36.03	30
1.60	22.21	24.87	30.85	
1.67	21.45	23.06	31.91	
1.75	19.41	18.91	31.97	
1.83	18.78	16.29	31.05	
1.92	17.63	14.85	33.30	
2.01	15.88	16.53	32.46	20
2.10	14.17	21.48	36.81	
2.20	15.74	21.76	33.53	
2.31	15.03	21.77	29.11	
2.42	13.65	20.92	25.56	
2.53	11.68	14.78	23.77	10
2.65	10.91	16.71	24.14	
2.78	9.80	17.66	21.25	
2.91	9.36	16.00	20.92	
3.05	8.02	14.03	19.49	
3.19	6.78	14.45	18.40	
3.34	6.87	12.45	17.53	
3.50	6.49	11.88	16.49	
3.66	5.67	10.31	16.04	
3.84	5.89	9.33	15.61	
4.02	5.22	8.98	13.62	
4.21	3.97	8.49	11.86	
4.40	3.13	7.65	10.10	
4.61	3.25	7.01	8.52	
4.83	3.31	6.50	7.55	
5.06	3.24	4.83	6.55	
5.30	2.99	3.80	5.91	
5.55	2.88	3.50	5.01	
5.81	3.06	3.13	4.31	15
6.09	3.36	3.22	3.96	
6.37	3.91	3.41	3.70	
6.67	4.51	3.37	3.55	
6.99	3.68	3.62	3.22	
7.32	1.69	3.62	2.69	30

7.66	0.00	2.86	2.40	
8.03	0.00	2.53	2.91	
8.41	0.00	2.85	3.81	
8.80	1.14	4.64	4.33	50
9.22	3.14	9.48	3.54	
9.65	4.00	1.31	2.63	100

References

1). A. G. Beyerle, in Neutron Cross Sections for Technology, ed. C. H. Johnson, (in press) and Bull. Am. Phys. Soc. 24 (1979) 866.

2). A. G. Beyerle et. al. ,Bull. Am. Phys. Soc. 25 (1980) 543.

3). H. H. Hogue, "Elastic and Inelastic Scattering of Fast Neutrons by ^{6}Li, ^{7}Li, ^{9}Be and ^{12}C", unpublished PhD dissertation, Duke University (1977).

4). S. G. Glendinning, "Elastic and Inelastic Neutron Scattering Cross Sections For ^{10}B, ^{11}B, and ^{16}O", unpublished PhD dissertation, Duke University (1980).

5). S. El-Kadi, et. al., in Neutron Cross Sections For Technology, ed. C. H. Johnson (in press) and Bull. Am. Phys. Soc. 24 (1979) 878.

6). J. H. Towle and R. O. Owen, Nuclear Physics, A100 (1967) 257.

7). David B. Thomson, Physical Review 129 (1963) 1649.

8). R. M. Wilenzick, et. al., Nuclear Physics 62 (1965) 511.

9). W. E. Kinney and F. Perey, ORNL-4515, Oak Ridge National Laboratory, 1963).

10). G. Stengl, M. Uhl, H. Vonach, Nuclear Physics A290 (1977) 109.

11). Suresh C. Mather, P. S. Buchanan, and I. L. Morgan,

Physical Review 186 (1969) 1038.

12). D. M. Drake, et. al., Nuclear Science and Engineering, 63 (1977) 401.

13). N. S. Biryukov, et. al., Soviet Journal of Nuclear Physics, 19 (1974) 608.

14). D. W. Glasgow et. al., National Bureau of Standards, Special Publication. 425, 1, (1975) 99.

15). L. W. Seagondollar, et. al., in Neutron Cross Sections for Technology ed. C. H. Johnson (in press) and Bull. Am. Phys. Soc. 24 (1979) 877.

16). TUNL Tritium Protection System, F. O. Purser, TUNL internal document.

17). M. Drosg, et. al., Nuclear Intruments and Methods, 140 (197) 515.

18). M. Drosg and G. F. Aughambaugh, Nuclear Instruments and Methods, 140, (1977) 515.

19). P. Thambidurai, et. al., Paper EB1, Program of the 47th Meeting the Southeastern Section of the American Physical Society (1980) 21.

20). D. W. Glasgow, D. E. Velkey, J. D. Brandenberger, M.T. McEllistrem, H. J. Henneck and D. V. Breitenbecher, Nuclear Instruments and Methods. 114 (1974) 521.

21). P. Sperr, H. Speiler, M. R. Maier, and D. Evers, A Simple Pulse-Shape Discrimination Circuit, Nuclear

Intruments and Methods 116 (1974) 55.

22). Pulse Shape Discriminator Model 2160 Operating Manual,Canberra Industries, Inc., Meriden Connecticut.

23). C. O. Rigoleur, F. G. Perey, and W. E. Kinney, ORNL-4523, Oak Ridge National Laboratory, Oak Ridge Tenn. (1970).

24). A. Horsley, Nuclear Data, 2 (1966) 243.

25). S. A. Cox, Nuclear Instruments and Methods. 56 (1967) 245.

26). W. E. Kinney, Nuclear Instruments and Methods. 83 (1970) 15.

27). D. E. Velkley, et. al., Nuclear Instruments and Methods. 129 (1975) 231.

28). Guide to the use of the EFFIGY Codes, H. H. Hogue and A. G. Beyerle, (unpublished).

29). H. H. Hogue and A. G. Beyerle, in Neutron Cross Sections for Technology, ed. C. H. Johnson, and Bull. Am. Phys. Soc. 24 (1979) 877.

30). Method of Statistical Testing, ed. Yu. A. Shreider, Elsevier Publishing Company, Amsterdam (1964).

31). The Monte Carlo Method, I. M. Sobol',translated by R. Messer, J. Stone, and P Fortini, The University of

Chicago Press, Chicago (1974).

32). Monte Carlo Principles and Neutron Transport Problems, Jerome Spanier and Ely M. Gelbard, Addison-Wesley Publishing Co., Reading, Mass. (1969).

33). Theoretical Nuclear Physics, John M. Blatt and Victor F. Weisskopf, John Wiley and Sons, New York, 1952.

34). Torleif Erikson, Advances in Physics 9 (1960) 425.

35). ENDF/B-V, BNL-NCS-50496, Brookhaven National Laboratory.

36). V. Weisskopf, Physical Review, 52 (1937) 295.

37). Vonach, private communication (1980).

38). P. Bevington, Data Reduction and Error Analysis for the Physical Sciences, McGraw-Hill Book Company, New York, 1969.